



OPEN ACCESS

EDITED BY

Zacharias Frontistis,
University of Western Macedonia, Greece

REVIEWED BY

Seyma Ozkara-Aydinoglu,
Beykent University, Türkiye
Jeremy Dhainaut,
Centre National de la Recherche
Scientifique (CNRS), France

*CORRESPONDENCE

Maria Laura Tummino,
✉ marialaura.tummino@stiima.cnr.it

RECEIVED 29 June 2023

ACCEPTED 21 August 2023

PUBLISHED 04 September 2023

CITATION

Tummino ML, Vineis C, Varesano A,
Liotta LF, Rigoletto M, Laurenti E and
Deganello F (2023),

$Sr_{0.85}Ce_{0.15}Fe_{0.67}Co_{0.33-x}Cu_xO_3$
perovskite oxides: effect of B-site copper
codoping on the physicochemical,
catalytic and antibacterial properties
upon UV or thermal activation.
Front. Environ. Eng. 2:1249931.
doi: 10.3389/fenv.2023.1249931

COPYRIGHT

© 2023 Tummino, Vineis, Varesano,
Liotta, Rigoletto, Laurenti and Deganello.
This is an open-access article distributed
under the terms of the [Creative
Commons Attribution License \(CC BY\)](https://creativecommons.org/licenses/by/4.0/).
The use, distribution or reproduction in
other forums is permitted, provided the
original author(s) and the copyright
owner(s) are credited and that the original
publication in this journal is cited, in
accordance with accepted academic
practice. No use, distribution or
reproduction is permitted which does not
comply with these terms.

$Sr_{0.85}Ce_{0.15}Fe_{0.67}Co_{0.33-x}Cu_xO_3$ perovskite oxides: effect of B-site copper codoping on the physicochemical, catalytic and antibacterial properties upon UV or thermal activation

Maria Laura Tummino^{1*}, Claudia Vineis¹, Alessio Varesano¹,
Leonarda Francesca Liotta², Monica Rigoletto³, Enzo Laurenti³
and Francesca Deganello²

¹Institute of Intelligent Industrial Technologies and Systems for Advanced Manufacturing, National Research Council of Italy (CNR-STIIMA), Biella, Italy, ²Institute for the Study of Nanostructured Materials, National Research Council of Italy (CNR-ISMN), Palermo, Italy, ³Department of Chemistry, Università di Torino, Turin, Italy

Perovskite-type compounds have found application in environmental remediation and in clean energy production, fundamental sectors for sustainable development. A challenge for these materials is the fine-tuning of their chemical composition and their chemical-physical characteristics, for example, microstructure, morphology and ability to form oxygen vacancies, through the introduction of dopant elements. In this work, we studied the effect of Cu doping at the B-site of a Ce, Co-doped strontium ferrate perovskite with chemical composition $Sr_{0.85}Ce_{0.15}Fe_{0.67}Co_{0.33}O_{3-\delta}$. Indeed, $Sr_{0.85}Ce_{0.15}Fe_{0.67}Co_{0.23}Cu_{0.10}O_{3-\delta}$ and $Sr_{0.85}Ce_{0.15}Fe_{0.67}Co_{0.13}Cu_{0.20}O_{3-\delta}$ powders, where the B-site was codoped with both cobalt and copper, were synthesised by solution combustion synthesis and characterised for their physicochemical properties by a multi-analytical approach, to assess their behaviour when subjected to different activation methods. The two codoped perovskites were tested 1) as catalysts in the oxidation of soot after activation at high temperatures, 2) as antibacterial agents in ambient conditions or activated by both UV exposure and low-temperature excitation to induce the generation of reactive species. Results demonstrated that these compounds react differently to various stimuli and that the increasing amount of copper, together with the presence of segregated ceria phase, influenced the materials' features and performances. The knowledge gained on the structure-properties relationships of these materials can inspire other research studies on perovskite oxides application as multifunctional materials for the benefit of the environment, society and economy.

KEYWORDS

strontium ferrate, codoping, soot oxidation, photocatalysis, thermocatalysis, antibacterial activity

1 Introduction

Perovskite oxides with the general formula ABO_3 belong to the ternary family of crystalline structures, in which A represents a large cation among alkaline/alkaline earth/rare earth metals and B is a small transition metal cation (Royer et al., 2014; Khirade and Raut, 2022). Perovskite-type oxides are widely studied due to their composition flexibility and interesting properties (Ishihara, 2017; Thomas and Balakrishnan, 2020), such as ionic conductivity, optical/magnetic features (Wu and Zhu, 2016; Khirade and Raut, 2022), sensing functionality (Bulemo and Kim, 2020; Soury and Salar Amoli, 2023), catalytic properties such as in oxidation (Bueno-López, 2015; Yang and Guo, 2018; Rojas-Cervantes and Castillejos, 2019), reduction (Kaur and Singh, 2020; Shen et al., 2021; Cao et al., 2022) and photocatalytic reactions (Das and Kandimalla, 2017; Lim et al., 2019; Mamba et al., 2022; Mabate et al., 2023; Wang et al., 2023), adsorptive (Das and Kandimalla, 2017; Njoku et al., 2022) and biological activity (Zhang et al., 2014; Thomas and Balakrishnan, 2020; Abdel-Khalek et al., 2021). They also display an electronic configuration from insulating to semiconductive and superconductive (Das and Kandimalla, 2017; Ishihara, 2017), which widens the possibilities for their use in a significant range of applications. For this reason, many efforts have been made to adapt the characteristics of these mixed oxides to each specific application, exploring various methods for their fine-tuning. In particular, it is possible to act on composition and cation charges (Grabowska, 2016; Thomas and Balakrishnan, 2020; Shen et al., 2021), crystal structure (Ikeda et al., 2016; Ishihara, 2017; Kaur and Singh, 2020; Mohammed et al., 2020; Kotomin et al., 2022), morphology (Neagu et al., 2013; Mohammed et al., 2020; Yu et al., 2020), oxygen vacancies (δ) and other defects (Eichel et al., 2013; Neagu et al., 2013; Bueno-López, 2015; Prakash and Jalan, 2019; Rojas-Cervantes and Castillejos, 2019; Bulemo and Kim, 2020; Ji et al., 2020; Zhang et al., 2021; Monama et al., 2022; Mi et al., 2023; Soury and Salar Amoli, 2023) by different strategies in terms of doping the A-/B-sites, compositing and choosing proper preparation methods (Wu and Zhu, 2016; Taylor et al., 2017; Deganello et al., 2018; Yang and Guo, 2018; Gainutdinov et al., 2019; Kaur and Singh, 2020; Walton, 2020; Xia et al., 2020; Su et al., 2021; Zhang et al., 2021; Monama et al., 2022).

A doped perovskite-type oxide can be described with formula $A_{(1-x)}A'_x B_{(1-y)}B'_y O_{3-\delta}$, where A' and B' are the doping elements, while x and y are the substituting fractions of the primal constitutive A and B cations (Royer et al., 2014). The substitution of A/B site cations of perovskites could also contribute to the formation of oxygen vacancies or cations' partial oxidation or reduction to maintain the electrical neutrality and oxide stoichiometry (Yang and Guo, 2018; Li et al., 2023b; Park et al., 2023), although some non-stoichiometric perovskite-based materials have been specifically prepared to obtain peculiar properties (Neagu et al., 2013; Shomrat et al., 2014; Liang et al., 2021; Su et al., 2021). Thanks to several possibilities to dope a perovskite without damaging its structural stability, the materials that can be created are countless. In the literature, the so-called codoping has also been explored, being intended as the presence of a dopant in both A- and B-site (Kang et al., 2013; Tonda et al., 2014; Guo et al., 2019; Li et al., 2020; She et al., 2022), but it has also been associated with the simultaneous substitution of the principal cation in either A- or B-site by two other

elements (Sun et al., 2015a; Lu et al., 2016; Cowin et al., 2017; Liu et al., 2018; Hoang et al., 2019; Yao et al., 2019; Song et al., 2020; Monama et al., 2022). In most of the cited works, both the connotations related to the incorporation of (at least) two different ions into the ABO_3 crystal lattice have been reported to be beneficial. In general, codoping allows exploiting the different ion synergy, leading to enriched features, such as charge separation efficiency, and modulated structure and microstructure up to a concentration limit when the properties start to deteriorate (Ahmad et al., 2018; Mamba et al., 2022; She et al., 2022). For instance, Tonda et al. (Tonda et al., 2014) codoped $SrTiO_3$ nanoparticles with lanthanum in A-site and chromium in B-site for photocatalytic applications. On the one hand, the studies revealed that the absorption edge shifted towards the visible light region after doping with Cr, which is highly advantageous for absorbing the visible light in the solar spectrum. On the other hand, La addition enhanced the degradation of Rhodamine B under sunlight irradiation, acting as a greatly effective donor for stabilizing Cr^{3+} in the perovskite lattice. Moreover, Cr,La-codoped $SrTiO_3$ nanoparticles possessed a high surface area (almost twice that of the pure $SrTiO_3$) and smaller crystallite size. Another example regards the use of $SrTi_{1-(x+y)}Mo_xV_yO_3$ in the methylene blue photobleaching under visible-light irradiation (Hoang et al., 2019). The authors reported that the improved efficiency of the codoped strontium titanate (with two substituting elements in the B-site) was due to Mo^{6+} and V^{5+} presence in the host lattice, which created impurity defect states, inducing the reduction of the semiconductor band gap energy.

In strontium ferrate ($SrFeO_3$ perovskite oxides), iron at the B-site has an unusual oxidation state of +4, whereas, in most ABO_3 perovskite oxides, it is +3 (Tummino, 2022; Lu et al., 2023). On the basis of temperature and partial pressure conditions, these perovskite-type oxides can accommodate an extensive range of oxygen deficiencies, undergoing crystal structural changes according to the δ values: from cubic at $\delta = 0$ to brownmillerite-type at $\delta = 0.5$ (Abd El-Naser et al., 2021). Such oxygen non-stoichiometry and structural versatility are essential factors in tuning, for example, oxygen adsorption and mobility. Additionally, through multiple doping, the $SrFeO_3$ properties can be successfully tuned for a better catalytic performance (Farr et al., 2020). These materials have been proposed in different technological fields, such as electrodes for electrochemical devices, oxygen exchangers, combustion catalysts, photocatalysts among others. In some of the mentioned applications, high temperatures or other external energy sources (e.g., light) are required to exploit material functionalities (Tummino, 2022).

For the design of the composition under examination in this paper, we started from previous knowledge of Ce-doped strontium ferrates. In particular, a $Sr_{0.85}Ce_{0.15}FeO_{3-\delta}$ was prepared by solution combustion synthesis (SCS), where cerium was chosen to induce the Fe^{4+} - Fe^{3+} couple (Fe^{3+} is generated as a consequence of the extra-positive charge in A-site to reach the electroneutrality) and to stabilise the octahedral Fe^{3+} site and the cubic environment, which is usually more efficient than other structures in catalytic applications (Trofimenko and Ullmann, 2000; Deganello et al., 2006; Fernández-Ropero et al., 2014). The material was tested as a photocatalyst in the presence of simulated solar light towards Orange II and Rhodamine B as model pollutants (Tummino

et al., 2017). Although strontium ferrate is known as a photocatalyst, good reactivity was highlighted in the 55°C–80°C temperature range without light irradiation, indicating that it can work as well in the dark as a thermocatalyst. Given this peculiarity, the study of this material was deepened by designing systems for the practical implementation of Ce-doped SrFeO_{3-δ} perovskites and their integration into the existing facilities for the depollution of real wastewater, also in combination with membrane filtration technologies (Janowska et al., 2020; Østergaard et al., 2021). Other materials were developed by adding cobalt at B-site beyond the A-site Ce substitution. The oxides were a series of Sr_{0.85}Ce_{0.15}Fe_{0.67}Co_{0.33}O_{3-δ}, which were prepared by SCS using mixtures of sucrose and polyethylene glycol with different molecular weights (PEG1000 and PEG 20000) as combustion fuels (Tummino et al., 2020). The materials were tested as cathodes for Intermediate Temperature-Solid Oxide Fuel Cells (IT-SOFC), namely, operating between 500°C–800°C (Shi et al., 2016). Cobalt-containing electrodes are known for their good electrochemical performances at low-intermediate operating temperatures because of their excellent activity in oxygen reduction/evolution reactions and electron conductivity (Li et al., 2019b; Wolf et al., 2023), although the sustainable challenge is to decrease the cobalt content in the catalysts, since cobalt has become a critical material (Gupta et al., 2023). In the case of Sr_{0.85}Ce_{0.15}Fe_{0.67}Co_{0.33}O_{3-δ}, the improvement of electrochemical features was driven by peculiar synthesis conditions and ascribed to the formation of high-valence iron and cobalt species at a low temperature plus the creation of nanostructured crystalline domains, which enhanced the oxygen exchange rate. Analogously, in other catalytic applications, cobalt presence was recognised as a favourable condition, taking into account the possibility to stabilise differently charged ions from 2+ to 4+, which can also coexist in the perovskite oxide (García-López et al., 2015; Cho et al., 2021; El Mragui et al., 2021; Ejsmont et al., 2022; Ponraj et al., 2022).

In this paper, we included copper at the B-site of Sr_{0.85}Ce_{0.15}Fe_{0.67}Co_{0.33}O_{3-δ} as an additional doping element to substitute the cobalt fraction of 0.33. Copper was chosen to enhance both the catalytic properties and the antibacterial activity of the Ce,Co-doped SrFeO₃. Copper oxides (Ali et al., 2020) and also perovskites with Cu at B-site (Deng et al., 2010; Cowin et al., 2017; Torregrosa-Rivero et al., 2019; Uppara et al., 2019; Vieten et al., 2019; Parmar et al., 2020; Sun et al., 2021) have gained much attention in heterogeneous catalysis, especially for oxidation reactions with active oxygen species, water-gas shift reactions, methanol synthesis, etc., showing fast electron transfer and oxygen exchange capacity. Copper ions are also largely utilised as antimicrobial agents, whose action mechanism is, however, debated. It has been reported that copper ions can 1) damage pathogens through physical interactions by puncturing microorganism membranes, 2) generate reactive oxygen species (ROS) through a Fenton-like mechanism, or 3) combine both actions inducing an oxidative stress response involving endogenous ROS (Salah et al., 2021). In order to evaluate the applicability of copper-doped Sr_{0.85}Ce_{0.15}Fe_{0.67}Co_{0.33}O_{3-δ} under different activation methods, they were tested in the oxidation of soot (high-temperature) and as antibacterial agents. The possibility of generating reactive species after the light exposition and after a

low-temperature triggering was also explored as an indicator of photo- and thermo-catalytic activities.

2 Materials and methods

2.1 Synthesis of the powders

The powders were prepared by solution combustion synthesis, using citric acid as a fuel (Deganello et al., 2009). To obtain about 2 g of the product, Sr(NO₃)₂ (anhydrous, ≥99.97% Alfa Aesar GmbH & Co. KG, Karlsruhe, Germany), Ce(NO₃)₃·6H₂O (99.99%, Sigma-Aldrich & Co., Saint Louis, MO 63103, United States), Co(NO₃)₂·6H₂O (99.99% Sigma-Aldrich & Co., Saint Louis, MO 63103, United States), Fe(NO₃)₃·9H₂O (99.99% Sigma-Aldrich & Co., Saint Louis, MO 63103, United States) and Cu(NO₃)₂·2.5H₂O (Sigma-Aldrich & Co., Saint Louis, MO 63103, United States) were first weighted. For the sample with composition Sr_{0.85}Ce_{0.15}Fe_{0.67}Co_{0.23}Cu_{0.10}O_{3-δ} (SCFCC10), the reactants were 1.7917 g of Sr(NO₃)₂, 0.6488 g of Ce(NO₃)₃·6H₂O, 0.6523 g of Co(NO₃)₂·6H₂O, 2.7164 g of Fe(NO₃)₃·9H₂O and 0.2317 g of Cu(NO₃)₂·2.5H₂O. For the sample Sr_{0.85}Ce_{0.15}Fe_{0.67}Co_{0.13}Cu_{0.20}O_{3-δ} (SCFCC20) the nitrates' weight were 1.7876 g of Sr(NO₃)₂, 0.6473 g of Ce(NO₃)₃·6H₂O, 0.3615 g of Co(NO₃)₂·6H₂O, 2.7102 g of Fe(NO₃)₃·9H₂O and 0.4622 g of Cu(NO₃)₂·2.5H₂O. The metal precursors were poured into a 1 L stainless steel beaker and dissolved in distilled water (200 mL) under magnetic stirring. Proper amounts of ammonium nitrate (≥99.5% BioXtra-Sigma-Aldrich Chemie GmbH, Schnellendorf, Germany) and citric acid (≥99.5%, anhydrous, Sigma BioUltra) were then added to the metal precursors' solution as additional oxidant and propellant-microstructural template-complexing agent, respectively. Both the fuel-to-metal cation molar ratio and the reducers/oxidisers ratio (Φ) were set to 2. The water was left to evaporate from the precursor solution at the controlled temperature of 80°C under constant magnetic stirring until the formation of a homogeneous sticky gel. The self-combustion reaction was triggered and initiated by setting the hotplate temperature to around 300°C (although the real temperature at the bottom of the stainless steel beaker was about 210°C). The as-burned powders were calcined in a muffle furnace (1,000°C/5 h) to crystallise the perovskite-type phase and eliminate the unburnt carbon residues derived from the combustion process. The materials were further washed prior to tests with MilliQ water (500 mg L⁻¹) under magnetical stirring for 2 h to remove the eventual residue derived from the citric acid in the combustion synthesis (Tummino et al., 2017).

2.2 Physicochemical characterisation

The temperature-time profiles of the combustion process were recorded during the burning phase by means of a K-type thermocouple (1.5 mm in diameter) coupled with a data logger (PICO technology), with a sampling velocity of 20 bits per second, connected to a computer with Picolog software.

SEM measurements were performed using an EVO10 Scanning Electron Microscope (SEM, Carl Zeiss Microscopy GmbH) with an acceleration voltage of 20 kV. The samples were sputter-coated with a 20 nm-thick gold layer in rarefied argon, using a Quorum SC7620 Sputter Coater.

X-ray diffraction (XRD) measurements were carried out on a Bruker-Siemens D5000 X-ray powder diffractometer equipped with a Kristalloflex 760 X-ray generator (Bruker AXS GmbH, Karlsruhe, Germany) and with a curved graphite monochromator using Cu K α radiation (40 kV/30 mA). The 2 θ step size was 0.03, the integration time was 3 s per step, and the 2 θ scan ranged from 10° to 90°. The powder diffraction patterns were analysed by Rietveld refinement using the GSAS II software (Toby and Von Dreele, 2013). As starting models, we used a recently published reference structure with a similar chemical composition but devoid of copper, Sr_{0.85}Ce_{0.15}Fe_{0.67}Co_{0.33}O₃ (ICDD database, card number 00-070-0407, GIA grant ID: 18-01), and CeO₂ (PDF card n° 01-075-8371). A Chebyshev polynomial function with eight coefficients was chosen for the background. In the structure refinement, lattice constants, sample displacement, thermal parameters, and crystallite size were considered variable parameters. A Pseudo-Voigt (sum of Gaussian and Lorentzian) shape function was used to fit the peak shape. The agreement between fitted and observed intensities, the R_w factor and χ^2 (GOF: Goodness-of-Fit), were acceptable (Toby, 2006).

The specific surface area values were determined by applying the Brunauer–Emmett–Teller (BET) method, in the range p/p_0 0.05–0.3, to the nitrogen adsorption isotherms registered at –196°C using Sorptomatic 1900 (Carlo Erba) instrument. The samples were pre-treated under vacuum at 250°C for 3 h prior to the measurements.

The reduction properties of the perovskite oxides were studied by temperature-programmed reduction (TPR) measurements. Experiments were conducted with a Micromeritics Autochem 2910 apparatus equipped with a thermal conductivity detector (TCD) (Micromeritics Instrument Corp., Norcross, Georgia, United States). Before starting the analyses, the catalyst (*ca.* 100 mg) was pre-treated, flowing a 5% vol O₂ in He gas mixture (30 mL min⁻¹) at 600°C (10°C min⁻¹) for 60 min to clean the surface and then cooling down in He flow (30 mL min⁻¹) up to room temperature. A 5 vol% H₂ in Ar gas mixture (30 mL min⁻¹) was used to reduce the sample by heating from room temperature to 1,050°C at the rate of 10°C min⁻¹. The hydrogen consumption associated with the TPR profile was determined by applying a calibration curve.

The thermal behaviour of the calcined samples, washed with MilliQ water, was investigated by thermogravimetric-differential thermal analysis TGA-DTA (as heat flow measure) and differential scanning calorimetry (DSC). For TGA analyses (Mettler Toledo TGA-DSC 1, Schwerzenbach, Switzerland), about 10 mg of the sample within an alumina pan was heated from 30°C to 900°C at a rate of 5°C min⁻¹ in nitrogen flow, 70 mL min⁻¹. The TGA in the air flow were conducted by slightly changing the parameters to be better compared with other tests (soot oxidation): 30°C–800°C, at a rate of 10°C min⁻¹ in 80 mL min⁻¹ of air flux. Derivative thermogravimetry (DTG) was used to identify the temperature of maximum mass-loss rates. Differential scanning calorimetry (DSC) was carried out with a DSC calorimeter (Mettler Toledo 821e, Schwerzenbach, Switzerland) calibrated by an indium standard. The calorimeter cell was flushed with 100 mL min⁻¹ nitrogen. The run was performed from 30°C to 500°C, at the heating rate of 5°C min⁻¹ and the mass sample was comprised between 5 and 10 mg. The data processing was conducted with STARe Software.

2.3 Testing

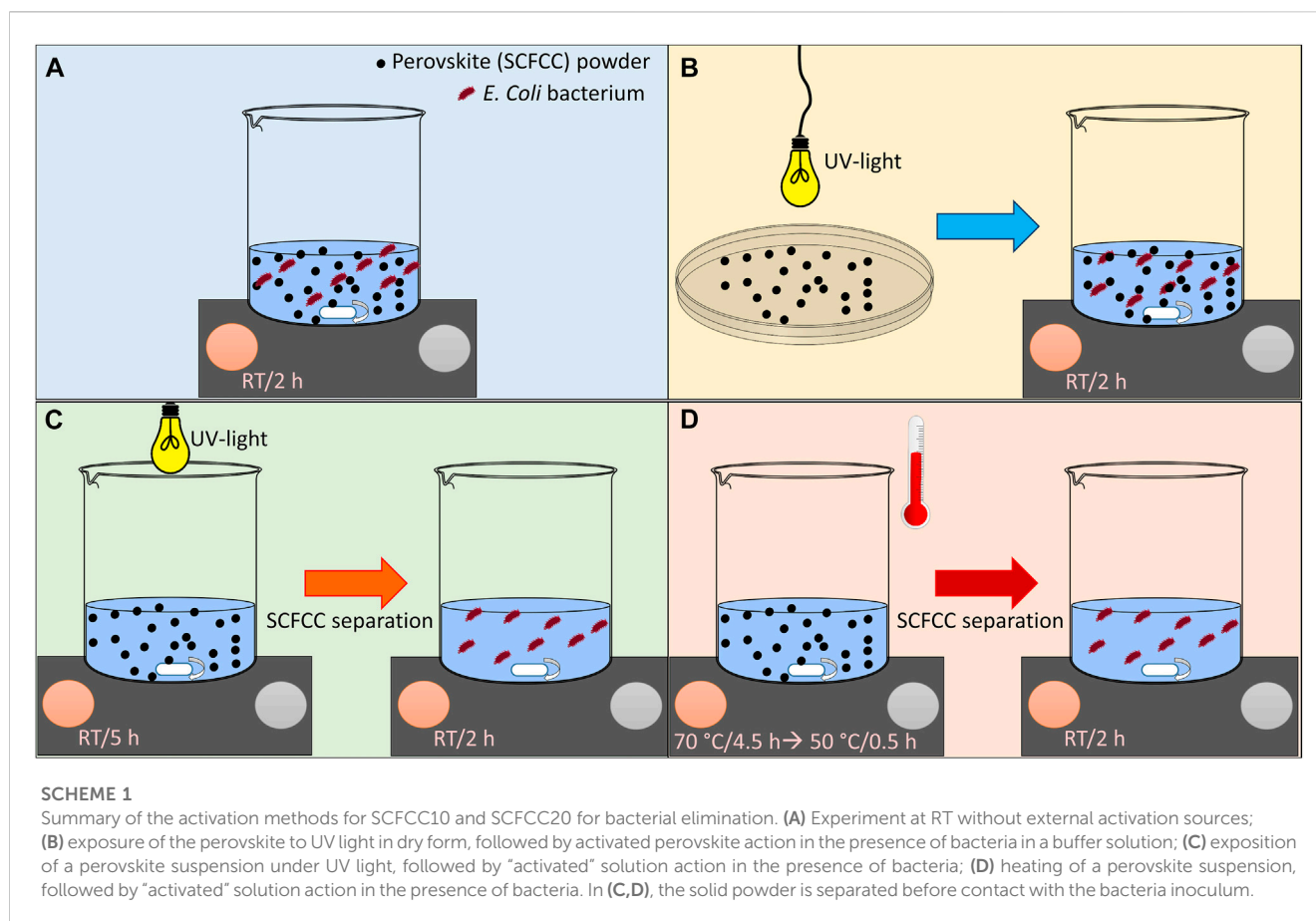
For the evaluation of the high-temperature catalytic activities in the oxidation of model soot (Carbon Black, Printex[®] U, Orion Engineered Carbons GmbH, Frankfurt, Germany), TGA was utilised as a combustion reactor (Reddy et al., 2008; Aneghi et al., 2014; Bueno-López, 2014; Aberkane et al., 2019) (30°C–800°C, at a rate of 10°C min⁻¹ in 80 mL min⁻¹ of air gas flow). In accordance with previous works (Zhang et al., 2016; Mahofa et al., 2018; Li et al., 2019a; Venkataswamy et al., 2019), the catalyst:soot ratio was set at 9:1. The activity of SCFCC10 and SCFCC20 was determined in both loose and tight modes. The tight mode implies an intimate contact between the catalyst and model soot, whereas the loose one presents poor contact between the compounds and is considered a more realistic condition (Bueno-López, 2014; Miceli et al., 2015; Zhang et al., 2016; Mahofa et al., 2018; Su et al., 2018; Aberkane et al., 2019; Venkataswamy et al., 2019; He et al., 2021b). For the loose contact mode, the catalyst and the soot were mixed with a spatula, whereas for the tight mode, the samples were homogenised in an agate mortar for 10 min.

Antibacterial activity was investigated in different conditions (Scheme 1). The general procedure follows the ASTM E 2149-2013 “Standard test method for determining the antimicrobial activity of immobilized antimicrobial agents under dynamic contact conditions.” This is a quantitative method performed under dynamic contact conditions. The bacteria were *Escherichia coli* ATCC 11229 (Gram-negative). The bacteria were grown in a proper nutrient broth (Buffered peptone water for microbiology, VWR Chemicals) for 24 h at 37°C. The bacteria concentration was measured with a spectrophotometer and diluted into a sterile buffer to give a 1.0–3.0 × 10⁵ CFU/mL working dilution. This bacterial inoculum was put in contact with the antibacterial agent (perovskite powder) under shaking at room temperature for 2 h (perovskite/inoculum ratio was 1g/50 mL), according to Scheme 1A. After this time, 1 mL of inoculum was diluted 1,000 times and plated in Petri dishes with Yeast Extract Agar (Sigma Aldrich). The Petri dishes were incubated 24 h at 37°C, and then, the surviving bacteria colonies were counted and compared to the initial bacteria concentration of the inoculum to calculate the % bacterial reduction using this equation (Eq. 1) (Blosi et al., 2021):

$$\text{Reduction (\%)} = \frac{(A - B) \times 100}{A} \quad (1)$$

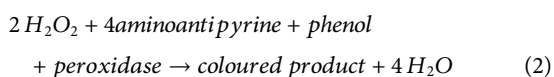
Where: A = number of viable microorganisms before treatment, B = number of viable microorganisms after treatment.

If this standard methodology describes the procedure at room temperature (RT) without any pre-treatment of the perovskite powders, three variants were tested. The first trials were carried out by activating SCFCC10 and SCFCC20 with UV light. Before contact with the bacteria inoculum, the materials were irradiated by an Osram Ultra Vitalux UV-A 300 W Lamp (Bonura et al., 2019) (distance from the samples = 20 cm) for 5 h either in dry form (Scheme 1B) or dispersed under stirring within a buffer solution (Scheme 1C). In this latter case, the bacteria inoculum was put in contact with the buffer solution after the separation of the solid catalyst to detect only the influence of the reactive species eventually generated (avoiding multiple events correlated to the perovskite powder activity). Considering the dilution effect given by the addition of the inoculum solution to the “activated solution,” the conditions were chosen to simulate the effect of 650 mg L⁻¹ of



perovskite suspension, recognised as a reasonable amount of material to produce reactive oxygen species able to degrade pollutants (Tummino et al., 2017). Analogously, the materials were subjected to another activation treatment triggered by temperature (Scheme 1D): a heating process (in the dark, under stirring) at 70°C for about 4.5 h was performed, and then the temperature was set to decrease to 50°C *max.* for further 30 min to avoid the thermal shock of the bacteria in the inoculum. Then, the antibacterial tests were performed, putting in contact the inoculum with the heated solution devoid of the solid powder.

For the evaluation of reactive species involved in the thermocatalytic approach, the samples were activated in water for 2 h at 70°C in a thermostatic bath. Hydrogen peroxide production tests were performed on the basis of the method proposed by Frew et al. (1983). In brief, a reactant solution was prepared by adding 0.234 g of phenol, 0.1 g of 4-aminoantipyrine, 1 mL of phosphate buffer 0.1 M pH 6.9 and 1 mg of horseradish peroxidase in 100 mL of bi-distilled water. Then, 1.5 mL of the sample solution (or of H₂O₂ standard solutions for the calibration curve) was added to 1 mL of reagent solution. After 5 min of stabilisation, the absorbance of the resulting solution was measured (Eq. 2). The red-purple-coloured product formed during the reaction is characterized by a molar absorptivity of 6.4x 10³ L mol⁻¹ cm⁻¹ at 505 nm.



Electron Paramagnetic Resonance (EPR)-spin trapping experiments were conducted to detect hydroxyl and superoxide anion radicals (Tummino et al., 2017). After 2 h of heating at 70°C, 0.017 mM 5,5-dimethyl-1-pyrroline-N-oxide (DMPO) was added to the suspension and maintained for 15 min at the same temperature, then the samples were transferred in capillary quartz tubes and the EPR spectra were recorded in a X-band Bruker EMX spectrometer. Experimental parameters were as follows: microwave frequency 9.86 GHz, microwave power 5 mW, modulation amplitude 1 Gauss.

In order to evaluate the stability of the materials in terms of metal ion release in solution, according to the procedure of Palma et al. (2023), we prepared a suspension of 650 mg L⁻¹ of SCFCC10 and SCFCC20 in distilled water and let it stir for 24 h. The solid powder was separated from the liquid by filtering with a syringe and a PVDF membrane (0.45 μm, Durapore[®], Millex[®], Merck Millipore Ltd. Tullagreen, Carrigtwohill, Co. Cork, IRL). The concentration of the metal ions (Sr, Fe, Co, Cu) was determined with an Inductively Coupled Plasma Optical Emission Spectrometer (ICP-OES, Optima 7000 DV, Perkin Elmer, MA, United States).

3 Results and discussion

3.1 Powder characterisation

It has been recognised that in SCS, the intensity of the combustion process, the reaction temperature and the amount

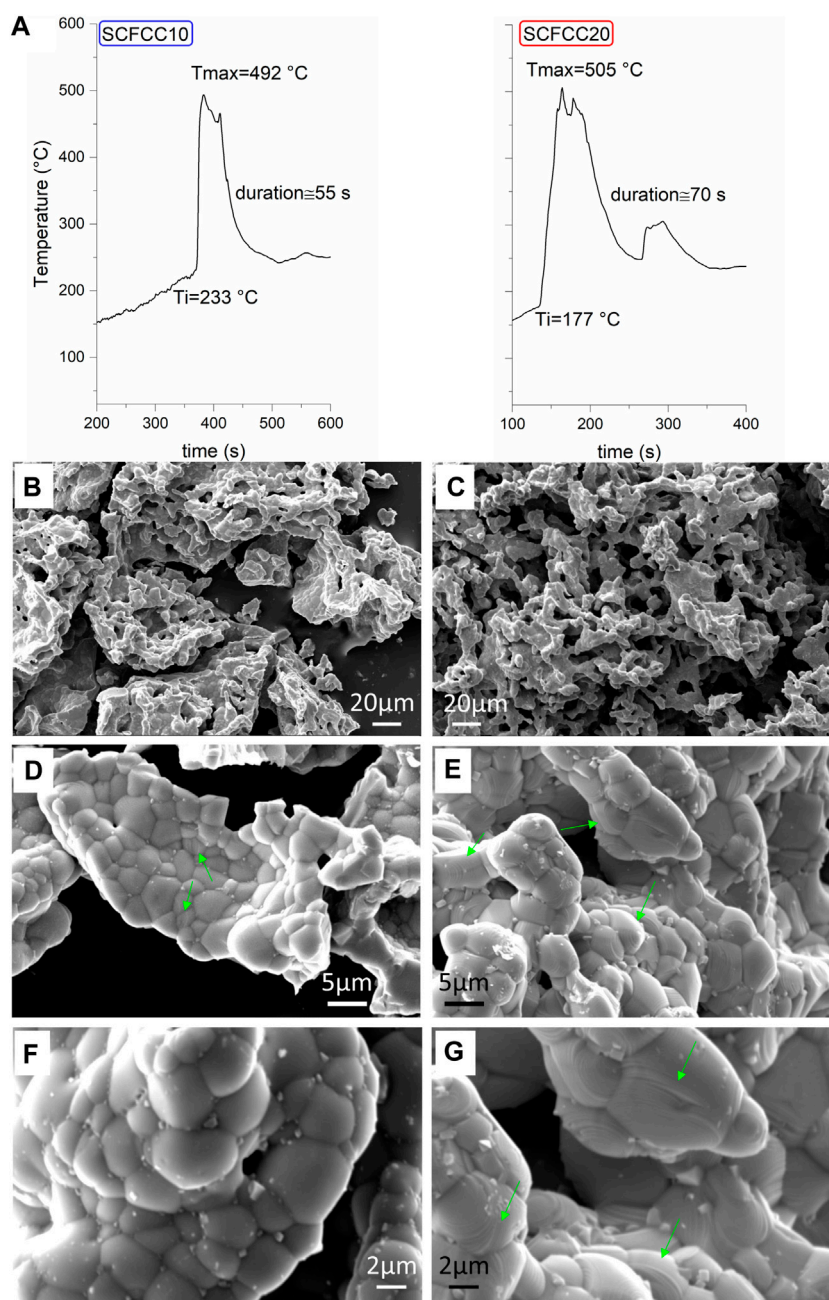


FIGURE 1

(A) Temperature-time profiles recorded during SCS; SEM images at different magnifications for SCFCC10 (B,D,F) and SCFCC20 (C,E,G). Green arrows in figures (D,E,G) indicate growth spirals/layers.

of evolved gases influence the morphological and textural properties of final materials, which are intimately correlated to the kinetics of particle formation (Deganello and Tyagi, 2018). Therefore, the SCS process was followed in the frame time of milliseconds by recording Temperature-time profiles with a thermocouple inserted in the gel. The parameters taken into account are the ignition temperature (Ti), defined as the lowest temperature at which the mixture takes fire and continues to burn, the maximum temperature of the combustion peak (Tmax), and the combustion duration, connected with the width of the peak (Figure 1A). The main step of the perovskite formation

starts at 233°C for SCFCC10 and at 177°C for SCFCC20, whereas the respective Tmax are 492°C and 505°C. The lowest temperature of ignition and the highest temperature of combustion peak in the case of SCFCC20 should denote a better efficiency of the combustion event (Deganello and Tyagi, 2018). However, the longer duration of the entire process in SCFCC20, together with the presence of an additional peak centred at about 300 s with Tmax 300°C, suggest a multi-step transformation of the precursors (Deganello et al., 2015). It is worth specifying that the hotplate temperature when the T-t recording started was higher in the case of SCFCC20 than in the case of SCFCC10.

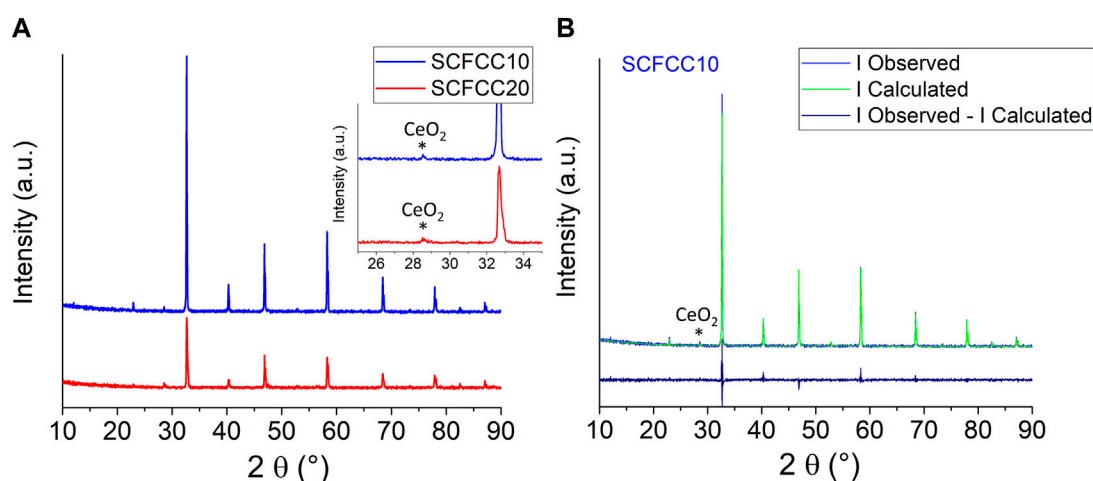


FIGURE 2

(A) XRD patterns of both examined samples and (B) graphical Rietveld refinement for SCFCC10. In (A), the inset displays a selected region of the diffractograms to highlight the presence of ceria phase at about 28.4° .

The specific surface area of both the copper-containing samples was below $5 \text{ m}^2 \text{ g}^{-1}$, as often occurs for Ce-doped SrFeO_3 (Palma et al., 2023). This value is in agreement with SEM images of SCFCC10 and SCFCC20 collected at lower magnification (Figures 1B, C, respectively), which confirm the presence of aggregates of particles with no evident porosities. With respect to other doped SrFeO_3 samples, which showed flake-shaped aggregates composed of irregular sub-micrometric spherical-like particles, forming void inter-particle space (Tummino et al., 2017; Tummino et al., 2020), here, the flake-like shape was lost, and sintering of the particles is strongly pronounced, suggesting that copper introduction might have promoted particle sintering (Amaveda et al., 2023). More in detail (Figure 1D), SCFCC10 presented aggregated particles with irregular shapes, from roundish to squared ones. The average length/diameter of particles is $3.5 \pm 1.6 \mu\text{m}$ [ca. five folds higher than other doped SrFeO_3 samples (Tummino et al., 2017; Tummino et al., 2020)]. In Figure 1D, green arrows indicate some circular bands that are evident on the particle surface. Concerning SCFCC20, the estimation of particle dimensions was less straightforward, since the particles seemed to have grown in different directions, like following a spiral pattern and creating sort of spherical polyhedrons.

Such aggregates are larger than in SCFCC10. The growth terraces of about a hundred nanometers in thickness (see some of them pointed out by green arrows in Figures 1E, G) presumably reflect the same phenomenon visible in SCFCC10, but with a high Cu-doping, it became more relevant. According to previous papers on other ceramics' stepped surfaces, these terraces can indicate that the growth of grains took place with either a two-dimensional (2D) layering mechanism or grain spiral growth (Liu et al., 2016; Garbarz-Glos et al., 2019). Zhang et al. (2022) noticed, as well, that Cu had a positive effect on the generation of defect points on the TiB_2/Al composites' particle surface, facilitating 2D nucleation and growth whose repeating contributed to the terraced morphology.

XRD outcomes are reported in Figure 2.

Rietveld Refinement results indicated that by incrementing the copper amount, the perovskite unit cell dimensions increased, as

already observed in the literature with other perovskite oxides (Cowin et al., 2017): the unit cell length was slightly larger (3.8727 ± 0.0001 and $3.8747 \pm 0.0003 \text{ \AA}$ for SCFCC10 and SCFCC20, respectively) and, accordingly, the cell volume expanded (from 58.08 ± 0.01 to $58.17 \pm 0.01 \text{ \AA}^3$). In fact, Cu^{2+} , the most common oxidation state of copper, has an ionic radius of 0.73 \AA under octahedral coordination (Nagrare and Bhoga, 2010; Renaudin et al., 2017), which is larger than Fe^{3+} high spin (0.645 \AA), Fe^{4+} (0.585 \AA), Co^{3+} low spin (0.545 \AA), and Co^{4+} high spin (0.53 \AA) in the same oxygen coordination. Thus, in a $\text{Sr}_{0.85}\text{Ce}_{0.15}\text{FeO}_3$ (whose volume is 58.5 \AA^3), the substitution of iron with cobalt decreased the cell dimension (bringing the volume to 57.8 \AA^3) (Tummino et al., 2017; Tummino et al., 2020), while copper addition enhanced it again. The crystallite size (CS) was estimated without considering the adjustment of microstrain, since, especially in the case of SCFCC20, the cubic structure seemed to be slightly distorted (Figure 2A), as similarly observed in (Østergaard et al., 2023). The CS values decreased in correspondence with higher Cu-doping levels, being $263 \pm 8 \text{ nm}$ for SCFCC10 and $111 \pm 4 \text{ nm}$ for SCFCC20. Moreover, both the materials were subjected to the segregation of CeO_2 out of the main perovskite phase (0.7 ± 0.1 and $2.6 \pm 0.2 \text{ wt.}\%$ for SCFCC10 and SCFCC20, respectively), where SCFCC20 resulted in losing about 20% of the A-site cerium content and presumably inducing a defectivity. On the contrary, no copper oxide was detected, given the absence of any peak at about 35° and 39° (Suresh et al., 2016). Cu-doping tolerance in SrFeO_3 was estimated to correspond to a substitution fraction ≤ 0.20 (Cowin et al., 2017; Vieten et al., 2019), whereas, in Co-doped SrFeO_3 , Ce was acceptable within the limit of ≤ 0.15 (Deganello et al., 2006; Tummino et al., 2020). Nevertheless, in the present case, the formation of another phase (ceria) beyond the main one was caused by the destabilisation of the perovskite structure due to the compresence/excess of two doping elements at the same time. It seems that cobalt and copper fully entered the perovskite structure, decreasing the perovskite A-site stability: indeed, Cu entered the perovskite B-site much better than how cerium could be stably

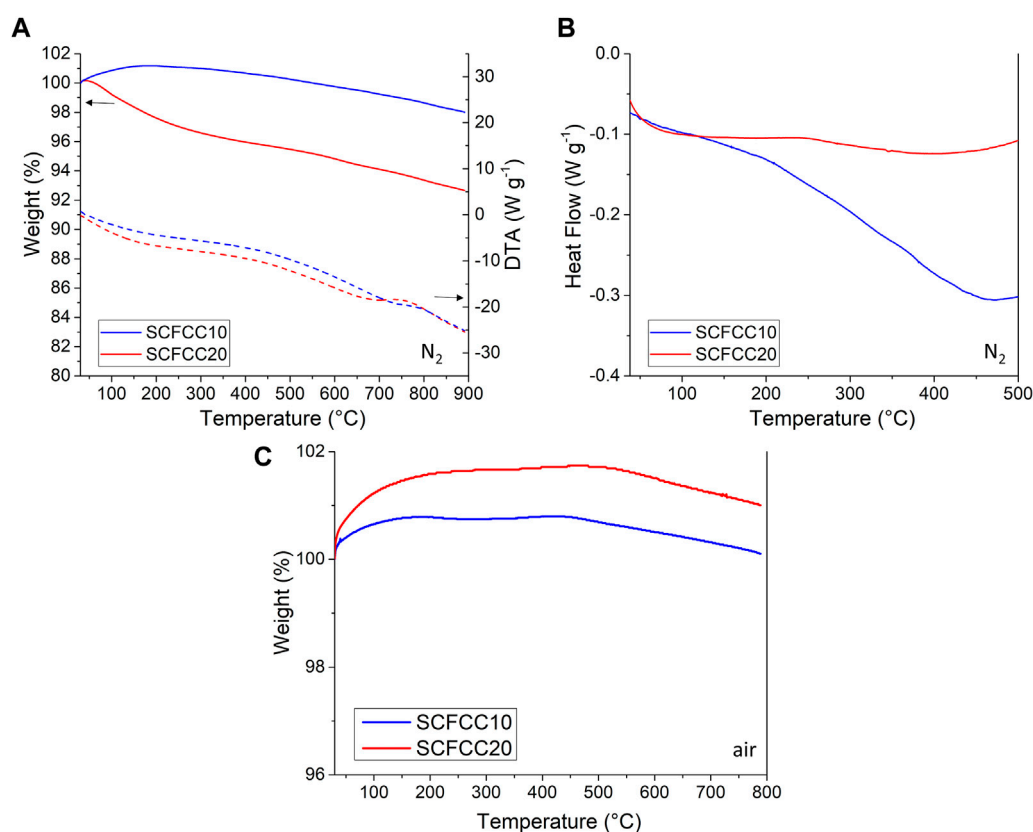


FIGURE 3

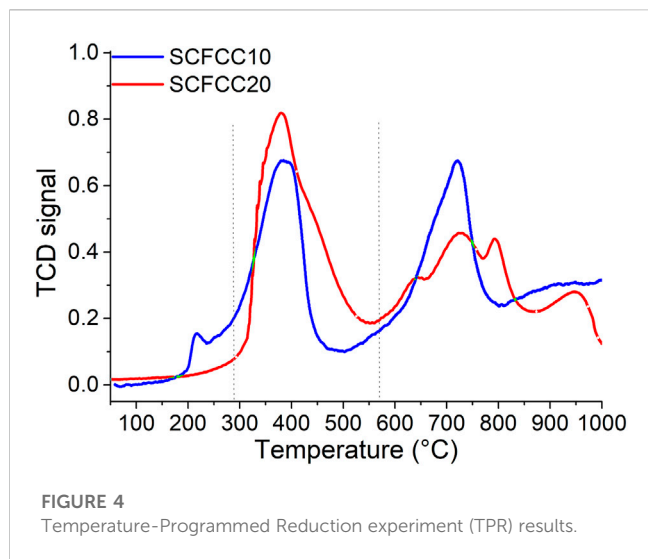
(A) TGA-DTA and (B) DSC results performed in nitrogen flow; (C) TGA carried out in air flow. In all cases different portions of calcined samples were used. In (A), solid curves are the weight loss trends, whereas dashed curves represent DTA (as heat flow measures); the black arrows indicate the y-axis to consider for the corresponding curves.

maintained at the A-site. Regarding the correlation between segregated phases and crystal size, it has been demonstrated that exsolved particles can nucleate and grow at the interface of the perovskite lattice, influencing its growth as well, and that the exsolution generally appears to be a stepwise, discrete process from a kinetic point of view (Neagu et al., 2019; Kwon et al., 2020). The precipitation of segregated phase particles in the examined samples can also be visualised in Figures 1D, E, where polyhedral-shaped particles along the perovskite grain boundaries are present, especially for SCFCC20 (Zhou et al., 2014; Garbarz-Glos et al., 2019).

The thermal behaviour of the calcined samples, washed with MilliQ water, was investigated by TGA-DTA and DSC (Figure 3). In Figure 3A, TGA between 30°C and 900°C under nitrogen are displayed. In the case of SCFCC10, a slight weight gain between ~100°C–300°C occurred, likely due to the so-called buoyancy effect (Amar et al., 2015; Saadatkhah et al., 2020), then, by further increasing the temperature up to 900°C the sample gradually lost a limited weight, around 2 wt%. Conversely, for SCFCC20, no weight gain occurred, and a mass decrease of ca. 6wt% was registered at 900°C. Despite the fact that the examined materials are inorganic compounds and were analysed after being washed, at first sight, it could be reasonable to hypothesise that residual organics from SCS were present in the powder and were subjected to thermal degradation, according to previous studies

(Deganello et al., 2015). Nevertheless, such weight loss trends were not confirmed by the TGA carried out in airflow over another portion of calcined samples (Figure 3C), which contrarily showed only a slight weight increment up to around 500°C, then, the mass decreased to around the original value of 100%.

If the weight increment phenomenon in the N₂ environment (that lasted up to 225°C max. in the case of SCFCC10, see Figure 3A) can be attributed to the buoyancy effect (Amar et al., 2015; Saadatkhah et al., 2020), a different circumstance can justify the weight gain in the case of air-TGA, which is correlatable to air oxygen absorption, favoured by the presence of O-vacancies typical of SrFeO₃ perovskite materials (Ikeda et al., 2016). However, in both N₂ and air-TGA, oxygen desorption events occur and are implied in weight losses (Figures 3A, C), especially starting from 450°C, when both mobile and lattice oxygen can be released (Cowin et al., 2017; Tummino et al., 2020; Górecka et al., 2022). DTA and DSC signals (which were complementary in the analysed temperature range and are presented in Figure 3A -dotted lines- and Figure 3B, respectively) also demonstrated signals/changes in slope at around 220°C–250°C, 450°C and 750°C–800°C, confirming the occurrence of the thermally-induced events already evidenced, which originate heat flow variations. In particular, at 750°C–800°C, other phenomena could be activated, connected to perovskite bulk O-lattice release (Dhakad et al., 2008; Cowin et al., 2017), or to the decomposition of a small amount of SrCO₃ that could be formed (although not detected



by XRD) and responsible for the weight loss with CO₂ release (Østergaard et al., 2022). Phase transitions are unlikely for such cubic perovskite oxides (Cowin et al., 2017), but it cannot be ruled out that the eventual A-site defectivity and the presence of CeO₂ segregated phase (with its important oxygen storage capacity) have contributed to oxygen mobility (Khalil et al., 2005; Fox et al., 2008; Huang et al., 2018; Li and Gao, 2018; Palma et al., 2023; Yang et al., 2023).

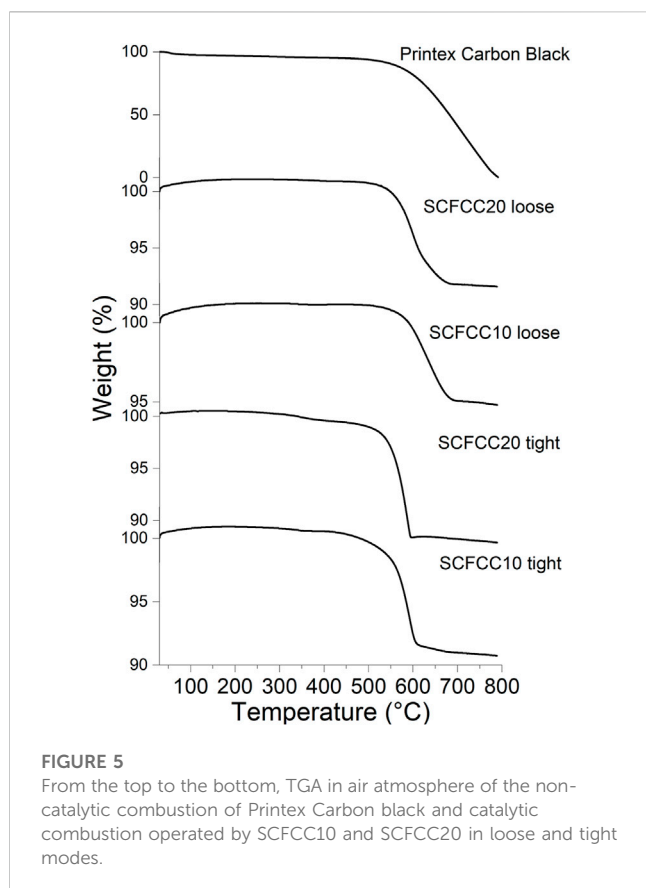
TPR measurements have been carried out to have information on the reduction properties of powders containing reducible cations. In Figure 4, the TPR profiles are reported, whereas the corresponding experimental H₂ consumptions are listed in Table 1. Given their different nominal composition, the two examined samples showed relatively different reduction behaviour, both from the qualitative and quantitative points of view. Indeed, from Figure 4, it is possible to observe that SCFCC10 possesses three main reduction regions that are in good agreement with the already obtained results for a Sr_{0.85}Ce_{0.15}Fe_{0.67}Co_{0.33}O_{3-δ} (Tummino et al., 2020). The reduction events in the low-temperature range (100°C–290°C) were ascribable to the presence of a certain amount of B-site cations with higher oxidation states, i.e., Fe⁴⁺ or Co⁴⁺. In the middle-temperature region (290°C–570°C), Co³⁺ to Co²⁺ and Co²⁺ to Co⁰ reduction processes occurred (peak centred at 400°C). In this range, also Cu²⁺ was reduced to Cu⁰ (Wang et al., 2020). The theoretical H₂ consumption for the complete reduction of Co³⁺ to Co⁰ and Cu²⁺ to Cu⁰ was calculated as 51 mL (H₂) g⁻¹, assuming that all the cobalt in the sample was present as Co³⁺. This value resulted in about a 10% decrement from the values registered for the SCFCC10, probably indicating that not all the

cobalt was found in the 3+ oxidation state. In the high-temperature region (570°C–1000°C), Fe³⁺ to Fe²⁺, Fe²⁺ to Fe⁰ and Ce⁴⁺ to Ce³⁺ reductions occurred (peak centred at 725°C). Therefore, the theoretical high-temperature H₂ consumption should be the sum of these contributions, namely, about 132.0 mL (H₂) g⁻¹. However, looking at Table 1, the consumption of H₂ was about 13% smaller than the theoretical one, probably because of the incomplete Fe²⁺ to Fe⁰ transformation, as demonstrated for other Ce-doped SrFeO₃ in previous papers (Deganello et al., 2006; Tummino et al., 2020) and, in agreement with the shape of the high-temperature peak that does not complete.

SCFCC20 TPR was devoid of the first peak related to high-valence cations, maintaining a certain correspondence in the reduction profile with the SCFCC10 one in the middle-temperature region where cobalt and copper reactions usually take place (peak centred at ca. 400°C with a shoulder at 450°C). However, by comparing the reduction curves and the H₂ consumptions listed in Table 1, for SCFCC20, the peak at about 400°C was notably more intense and the reduction features in the range 570°C–950°C were broader and with a lower H₂ consumption with respect to SCFCC10. Based on the experimental hydrogen consumption, it can be argued that the peak centred at ca. 400°C accounts for the concomitant reduction of some Fe⁴⁺/Fe³⁺, of Co³⁺/Co²⁺/Co⁰ and Cu²⁺/Cu⁰. Assuming that all cobalt is in the oxidation state 3+, the overall reduction Co³⁺ to Co⁰ requires around 23 mL (H₂)/g, then, the reduction Cu²⁺ to Cu⁰ consumes about 21 mL (H₂)/g, and, in total, the theoretical consumption for the above reduction steps should be 44 mL (H₂)/g. Considering that the experimental hydrogen consumption is equal to 62 mL/g for the first peak, it can be assumed that the remaining 18 mL/g may account for the reduction of some Fe⁴⁺ to Fe³⁺ (at temperatures higher than usual) and then to Fe²⁺. Indeed, as often happens in strontium ferrates, it is likely that some iron cations were stabilised into the structure preferentially as Fe⁴⁺ oxidation state (according to the smaller ionic radius of Fe⁴⁺ than Fe³⁺). It is worth noting that the so far reported theoretical calculations are only a hypothetical approach and we cannot estimate the real oxidation state of the cations only on the basis of the hydrogen consumption. Moreover, we have to take into account that the shoulder at 450°C is ascribable to the surface reduction of the segregated ceria oxide present in such sample, and, being the theoretical hydrogen consumption for reducing all Ce⁴⁺ to Ce³⁺ of around 9 mL/g, a few mL should be due to ceria surface. Concerning the high-temperature range above 570°C, three peaks, plus an additional one at approximately 950°C, were detected. As stated for the sample SCFCC10, at such temperatures, the reduction of iron and cerium cations within the perovskite lattice occurred, namely, some Fe³⁺ and Fe²⁺ to Fe⁰ and Ce⁴⁺ to Ce³⁺. Moreover, the reduction of Ce⁴⁺ present in the ceria bulk phase also takes place. Since the theoretical H₂ consumption for the over-reduction of Fe³⁺

TABLE 1 H₂ consumptions derived from TPR characterisation.

| Sample | H ₂ consumption (mL g ⁻¹) per range of temperature | | | Total H ₂ consumption (mL g ⁻¹) |
|---------|---|-------------|---------------|--|
| | 100°C–290°C | 290°C–570°C | 570°C–1,000°C | |
| SCFCC10 | 10 | 46 | 107 | 163 |
| SCFCC20 | — | 62 | 90 | 152 |



to Fe^{2+} is 41 mL/g and for the further step Fe^{2+} to Fe^0 is equal to 82 mL/g and taking into account the bulk ceria reduction, the experimental value of 90 mL/g may partially explain such reduction events but, once again, the reduction Fe^{2+} to Fe^0 resulted incomplete.

Globally, comparing the TPR results with thermal analyses (TGA and DSC), it is reasonable to find a correlation on the basis of the temperatures in which oxidation and reduction events occur, making them ascribable to the capacity of the materials to react through oxygen vacancies-driven mechanism and oxidability/reducibility of the different cations.

3.2 Powder testing: high-temperature activation for carbon oxidation

The catalytic activity of the oxide particles for the oxidation of model soot (Printex[®] Carbon Black) in the air atmosphere is presented by the TGA curves in comparison with bare Carbon Black (Figure 5). First, the shape of the curves changed in dependence on the type of perovskite powder and the contact mode (loose/tight). Three parameters have been taken into account to numerically evaluate the effect of SCFCC catalysts in the oxidation of the model soot: 1) the onset temperature (the point of intersection of the starting-mass baseline and the tangent to the TGA curve at the point of maximum gradient), 2) the end of the oxidative phenomenon (where the weight loss becomes irrelevant) and 3) the peak of DTG (first derivative of TGA).

In the case of the end of the oxidative phenomenon for Printex[®] Carbon Black, the considered value was 800°C, where the residual mass approached zero. The results related to these data are summarised in the histograms of Figure 6. It is distinctly observable that the onset temperature of the model soot oxidation in the absence of a catalyst (575°C) was reduced when the soot was mixed with the two B-site codoped strontium ferrate samples, as shown in Figure 6A. This was particularly true in the cases of the catalytic processes conducted by inducing the intimate contact between the soot and the catalyst (tight mode) and when the perovskite with the highest copper doping was used. A similar trend is recognisable by looking at the temperatures at which the oxidation ends: in particular, SCFCC20 (tight mode) completed its catalytic activity in the shortest temperature range (Figure 6B). The maximum of the DTG signal, which indicates the temperature at which the maximum degradation/oxidation rate occurs, was centred at 715°C in the broad peak of the bare Carbon Black, whereas it decreased by about 75°C in the presence of SCFCC10 in loose contact mode, up to diminishing of ca. 120°C in all the other catalysed processes (Figure 6C). The DTG trend is also in good agreement with DTA signals recorded in association with TGA. The general mechanism for soot oxidation over the catalysts firstly involves gaseous O_2 adsorption on their surface that, exploiting the filling-releasing process of the vacancies, can then form mobile oxygen species able to oxidize the soot (Dhakad et al., 2008; Mahofa et al., 2018; Sun et al., 2020). For the examined materials, this mechanism can be facilitated by the enhanced interaction with air oxygen, particularly when employing the perovskite richest in copper (see TGA in Figure 3C and the linked interpretation).

Another important aspect to consider is the relationship between performances and the doping amount (Sun et al., 2020; Khobragade et al., 2021), which, within the present study, also implies the influence of phase segregation. In general, the highest codoping level within the SrFeO_3 lattice brought a faster combustion at lower temperatures due to the favourable conditions related to oxygen vacancies and electronic interactions among the SCFCC cations occurring through redox reactions (see TPR results) (Li et al., 2019a; Sun et al., 2020; Górecka et al., 2022). Still, it is reasonable that the copresence of the perovskite with cerium oxide could have positively influenced the catalytic efficiency, as revealed in the case of SCFCC20, where exsolved ceria was quantitatively significant. Indeed, the DTG of the SCFCC20-catalysed soot combustion in loose contact (data not shown) is composed of a sharper peak followed by a shoulder, whose deconvolution underlies the contribution of three peaks (centred at $592^\circ\text{C} \pm 4^\circ\text{C}$, $594^\circ\text{C} \pm 6^\circ\text{C}$, $652^\circ\text{C} \pm 6^\circ\text{C}$), that might reflect the different reaction steps due to the copresence of the phases constituting the material (Kastrinaki et al., 2015). From this point of view, the literature supports such a hypothesis regarding the advantageous synergy of coexistent phases and specifically for Ce and Cu-based catalytic compounds (Fox et al., 2008; Rao et al., 2011; Mahofa et al., 2018; Venkataswamy et al., 2019; Yang et al., 2019; Singh and Singh, 2020). This synergy factor has been expected for some materials which have been purposely designed to originate *in situ* composites thanks to the exsolution of segregated phases or metal nanoparticles, as widely

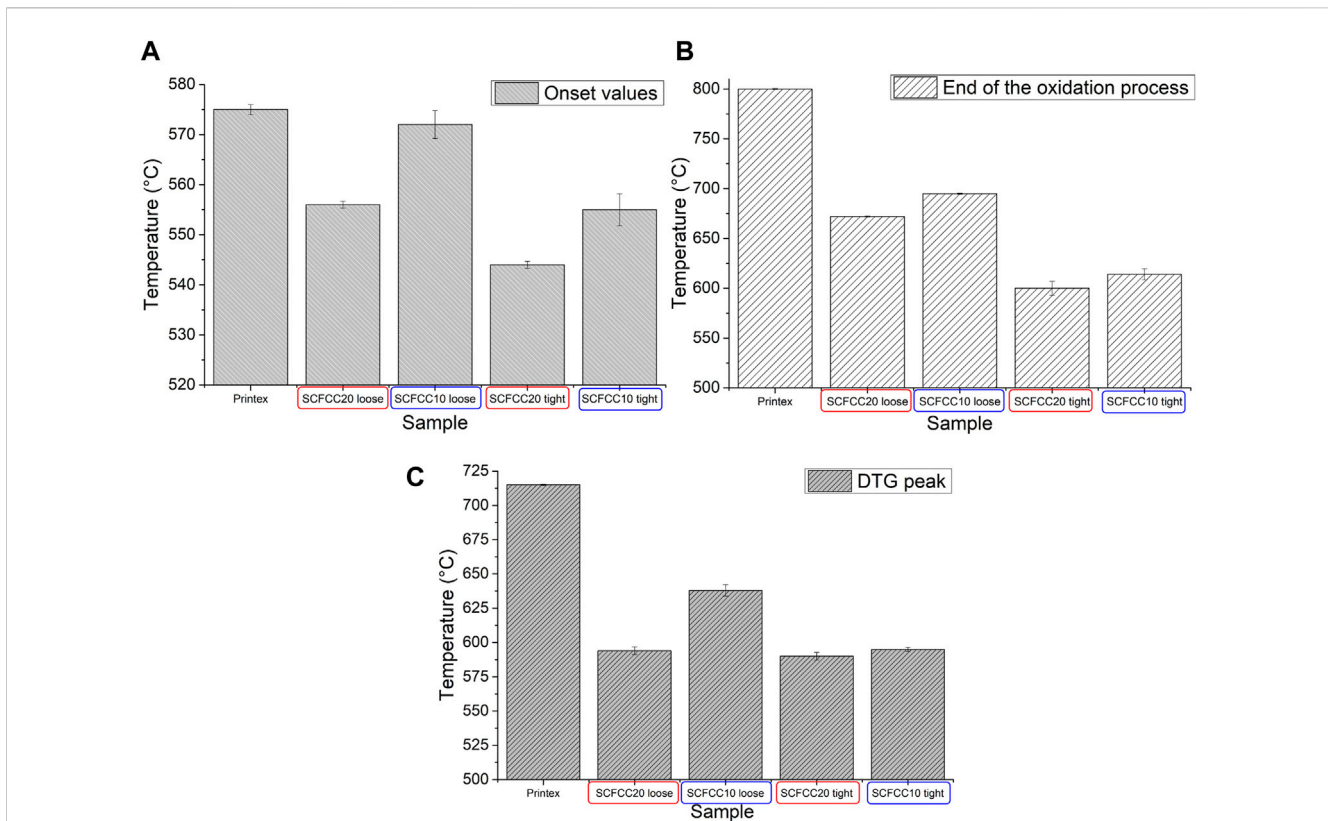


FIGURE 6 Histograms representing the TGA onset temperature (A), the end of the oxidative phenomenon (B) and the peak of DTG (C). In all the graphs, SCFCC10 is evidenced by blue and SCFCC20 by red and the sample order is: Printex Carbon Black (non-catalysed combustion), followed by catalysed processes in the presence of SCFCC20 (loose mode), SCFCC10 (loose mode), SCFCC20 (tight mode) and SCFCC10 (tight mode).

TABLE 2 Comparison of soot catalytic oxidation of SCFCC20 and other perovskites described in the literature.

| Sample | Synthesis | ΔT_{max} | ΔT_{fin} | Reference | Notes |
|--|------------------------------------|------------------|------------------|---------------------------------|--|
| SCFCC20 | SCS-Citric acid | 120 | 200 | This work | ΔT_{max} stands for the ΔT_{DTG} |
| GdFe _{0.7} Cu _{0.3} O ₃ | EDTA-Citrate | 164 | 128 | Uppara et al. (2019) | Tight mode; T_{max} = maximal soot combustion temperature |
| SrFe _{0.9} Mn _{0.1} O ₃ | Coprecipitation | 120 | N.A. | Khobragade et al. (2021) | Tight mode |
| Sr _{0.8} Ce _{0.2} CoO ₃ | Coprecipitation | 130 | 120 | Dhakad et al. (2008) | Loose mode; T_{max} considered as $T_{50\%}$ carbon combustion |
| La _{0.85} Ce _{0.15} CoO ₃ | Glycol/methanol complex-combustion | 146 | 142 | Sun et al. (2020) | Loose mode; T_{max} considered as $T_{50\%}$ soot conversion; T_{fin} considered as $T_{90\%}$ soot conversion |
| BaFeO ₃ | Citrate sol-gel | 69 | N.A. | Torregrosa-Rivero et al. (2019) | Loose mode; diesel soot oxidation assisted by NO ₂ ; T_{max} considered as $T_{50\%}$ soot conversion |

studied (Neagu et al., 2013; Sun et al., 2015b; Kwon et al., 2020; Li et al., 2020; Song et al., 2020).

In the literature, the application of perovskite catalysts for carbon oxidation has been explored: Table 2 compares some of them to the Sr_{0.85}Ce_{0.15}Fe_{0.67}Co_{0.13}Cu_{0.20}O₃ composition (SCFCC20 in tight mode) as the material with the highest activity presented in this work. The parameters taken into account are: 1) the synthesis method, 2) the ΔT_{max} as the temperature difference (°C) between the main thermal-induced

carbon oxidation phenomenon detected for the bare soot with respect to the catalysed process in the presence of the perovskite and 3) the ΔT_{fin} as the temperature difference (°C) between the end of the carbon oxidation reaction detected for the bare soot with respect to the catalysed process in the presence of the perovskite.

The table shows that the materials prepared herein are aligned and, in certain cases, more performing than other perovskites containing strontium, cerium, iron, cobalt and copper.

TABLE 3 Antibacterial test outcomes in terms of *E. coli* reduction (%) for the different experiment types A, B, C and D (accompanied by a brief description; for more details, see Section 2).

| Experiment type | Bacterial reduction (%) | |
|---|-------------------------|-----------------|
| | SCFCC10 | SCFCC20 |
| A—Powder suspension at RT | 26 | 55 |
| B—Powder at RT (dry) + UV (resuspended) | 0 | 0 |
| C—Powder at RT + UV (solution) | 71 | 98 |
| D—Powder at RT + heat (solution) | 33 ^a | 40 ^a |

^aThese data are reported as net of a reference value of bacteria reduction obtained in an *ad hoc* trial using heated distilled water alone (ca. 50°C).

3.3 Powder testing: antibacterial performances under different activating conditions

According to the procedures elucidated in the Section 2 (Scheme 1), different antibacterial tests against *E. coli* were carried out. The results are reported in Table 3.

The antibacterial efficiency of codoped strontium ferrates in experiment A, in which the bacteria were directly in contact with the perovskite powder, resulted in a very weak response of SCFCC10, whereas the activity began to be significant for SCFCC20. In a previous paper (Abdel-Khalek et al., 2021), SrFeO_{3-δ} nanoparticles were demonstrated to be applicable in fighting different pathogens (bacteria and fungi): the suggested mechanism principally implied the surface reactivity given by 1) the nano-sized structure that physically favoured the interaction microorganism-perovskite, 2) perovskite cations' exposed charges able to damage the cell membrane, 3) favourable electronic state occupancy in the presence of cations with multiple oxidation states and 4) oxygen vacancies. If all these factors inherent to the strontium ferrate features can influence the perovskite oxides performances, in this work, the best activity was found in association with the highest copper content, although it can also be imputed to the synergy with ceria. Indeed, also CeO₂ nanoparticles were proven as effective antibacterial agents owing to their reversible conversion of oxidation states Ce³⁺ - Ce⁴⁺ (Qi et al., 2020). Moreover, herein the targets (*E. coli*) are gram-negative bacteria whose cell wall is constituted by a thin peptidoglycan layer adjacent to the cytoplasmic membrane and an outer membrane composed of phospholipids and lipopolysaccharides, rich in anionic groups (e.g., carboxyl and phosphate) (Lopez-Romero et al., 2015). Therefore, the functionality of perovskite cations (positively-charged Sr, Ce, Fe, Co, Cu and the related redox couples) is reasonably exploited via the electrostatic interaction with the negatively-charged groups of cell membranes (Singh et al., 2017).

The above-mentioned bacterial reduction trend between the two samples was maintained when the Cu-containing perovskite oxide powders underwent UV exposure (experiment C), but with remarkably enhanced efficiency. The “activated” solution was capable of abating bacteria, reflecting the photosensitivity of the materials. On the contrary, the powders activated in the dry form and subsequently soaked in contact with *E. coli* lost their antimicrobial power (experiment B). The cause of this evidence is not totally clear. Indeed, semiconductors, including iron-based perovskites, have already been used as heterogeneous photocatalysts for inducing reactions in the

gas phase, for instance, exploiting the air humidity and atmospheric oxygen to form ROS (Jeong et al., 2013; Parrino et al., 2016; Zhang et al., 2018; Weon et al., 2019; He et al., 2021a; Sharma et al., 2022). In this work, the ambient lab conditions were stably set with 65% ± 5% of relative humidity, therefore in feasible conditions to have available oxygen for the adsorption and activation. We are prone to exclude that the step of dry UV-light exposure in the air has deactivated the material due to atmospheric water saturation of the active sites (since they would have been “freed” after perovskite soaking in the inoculum) (Jaison et al., 2023). Furthermore, it is hard to imagine that an eventual electron/hole recombination process in the dry form (Sharma et al., 2022) was irreversible after removing the excitation source and putting the material in a liquid medium. What can be supposed, instead, is a UV-promoted increment of the carbonate formation derived from atmospheric CO₂ (Wu and Huang, 2010; Østergaard et al., 2022), that hindered the catalytic processes even when suspended in the buffer solution containing bacteria. Actually, it has already been observed for a parent composition of Ce-doped SrFeO₃ photo-/thermocatalyst that strontium carbonate has a negative influence on the performances (Palma et al., 2023). A TGA analysis performed on a UV-irradiated sample (SCFCC20) has corroborated such a hypothesis, since the weight loss at 900°C almost doubled (from 6% to 11%) and also the trend of the TGA curve changed (with a steeper slope after 400°C), confirming the impact of the UV light on the material in the dry form.

Lastly, experiment D, conducted similarly to experiment C but involving the thermally-activation stage instead of light, showed a modest level of bacterial reduction. Compared to the recognised light-induced activity of strontium ferrates, the properties correlated to reactive species generation during the heating needed to be deepened to assess the thermocatalytic behaviour of the examined Cu-containing materials.

The formation of ROS during the thermocatalytic activation of perovskites was previously reported (Tummino et al., 2017; Palma et al., 2023). Therefore, after heating at 70°C a suspension of SCFCC10 or SCFCC20, we performed both EPR experiments in the presence of the spin trap DMPO, to reveal the presence of superoxide anion and hydroxyl radicals, and the colourimetric evaluation of hydrogen peroxide (Frew et al., 1983). EPR experiments showed the production of a small amount of •OH radical for both the sample, together with the production of secondary radicals, probably due to organic impurities still present in the samples or carbon dioxide radical anion (in Figure 7, SCFCC10 EPR spectrum is depicted as an example) (Villamena et al., 2006). On the contrary, the presence of O₂^{•-} was not observed in either of the two samples. On the other hand,

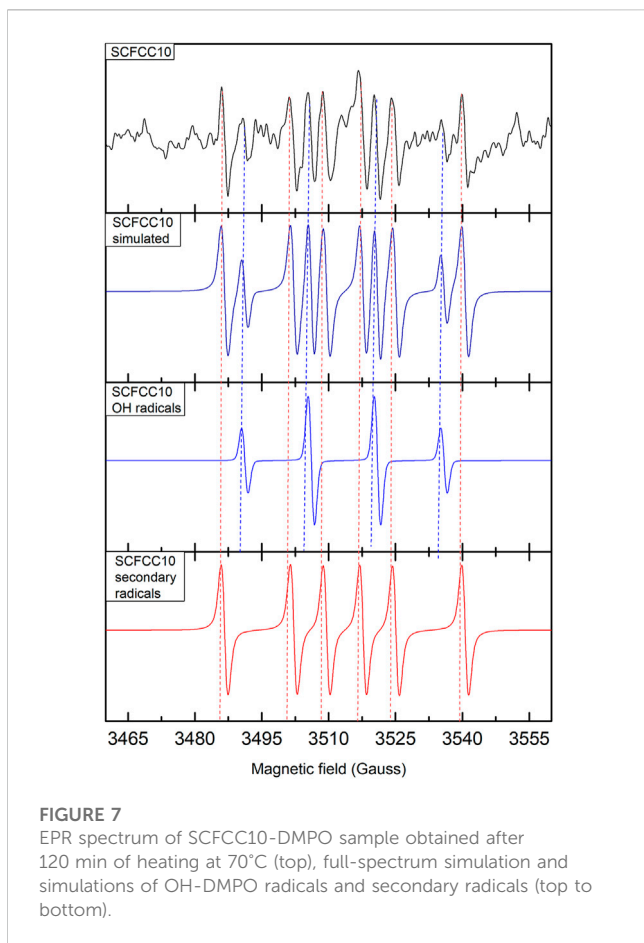


FIGURE 7
EPR spectrum of SCFCC10-DMPO sample obtained after 120 min of heating at 70°C (top), full-spectrum simulation and simulations of OH-DMPO radicals and secondary radicals (top to bottom).

the results obtained from the method proposed by Frew et al. (1983) showed the formation of an amount of H_2O_2 comprised between 2 and 3 μM during the heating. Although in such a relatively small value, H_2O_2 , beyond acting as an oxidant species, when it is in the eventual presence of Cu^{2+} , Fe^{2+} and Co^{2+} released from the perovskite, could have initiated a homogeneous Fenton-like reaction, as already observed in Salazar et al. (2012), Bianco Prevot et al. (2021), Li et al. (2023a). In order to evaluate this aspect, the released Sr, Fe, Co and Cu ions were estimated, finding that for SCFCC10 their quantities were, respectively, 308, 2.3, 2.4 and 8.4 $\mu\text{g L}^{-1}$ and for SCFCC20 they were 349, 27, 2.7, 25 $\mu\text{g L}^{-1}$. These exiguous quantities made us consider both materials very stable in suspension and exclude a significant role of ion species in the homogeneous phase (Maleki Rizi et al., 2019; Shokri and Fard, 2022). In any case, the limited formation of peroxide can explain the reduced thermocatalytic activity both with respect to the Cu-doped materials' photocatalytic process and to B-site undoped $\text{Sr}_{0.85}\text{Ce}_{0.15}\text{FeO}_{3-\delta}$ performances (Tummino et al., 2017; Palma et al., 2023). A quenching-like mechanism due to the temperature rise in relation to the enhanced oxygen filling/release steps within the two materials can play a role in poor thermal activation. Indeed, the careful regulation of oxygen vacancies has been recently demonstrated as a crucial parameter to optimise ROS action: Li et al. (2022) have found that too high or too low surface oxygen vacancies' concentration in an A-site-deficient CaFeO_3 was not conducive to the activation of H_2O_2 to produce $\cdot\text{OH}$ and may cause

hydrogen peroxide to decompose into H_2O or other weak free radicals.

The comparison of the presented materials with other iron perovskite oxides regarding the antibacterial activity is not straightforward, since the research on perovskite in this field is limited and methods used for antimicrobial activity determination are different. However, the first remark can be made analysing the work of (Abdel-Khalek et al., 2021), who used a non-doped Strontium Ferrate and found powerful bactericidal and fungicidal properties against a significant range of microorganisms: Gram-positive bacteria (*Bacillus subtilis* and *Staphylococcus aureus*), Gram-negative bacteria (*Escherichia coli*, *Pseudomonas aeruginosa*, *Enterococcus faecalis*, *Salmonella typhi*) and fungi strains (*Candida albicans* and *Aspergillus brasiliensis*). This versatility leads us to imagine that our codoped SrFeO_3 can also be applied in the future to eliminate different kinds of pathogens. Moreover, among iron-containing perovskites, $\text{La}_x\text{K}_{1-x}\text{FeO}_3$ (singh and Rakesh, 2019) and $\text{SrTi}_{1-x}\text{Fe}_x\text{O}_3$ (Zhang et al., 2014) have been investigated in the literature. In the latter case, in particular, *Escherichia coli* was fought in the presence of the perovskite oxide both in the dark and under visible light, but the authors pointed out the importance of the contact time as a fundamental parameter to exploit the bactericidal activity of generated ROS when the bacteria concentration was higher. Another interesting study is represented by the use of a BiFeO_3 (BFO) synthesised by the auto-combustion method using different amounts of Bi as starting precursors (0, 2, 5% of excess Bi) and honey as a combustion fuel (Sharmila et al., 2022). The so-prepared BFO nanoparticles showed both visible light-photocatalytic properties and antibacterial features against *Staphylococcus aureus* and *Escherichia coli*. The material synthesised with a 2% excess of Bi in the BFO nanoparticles was the most efficient, in particular against *E. coli*, confirming the importance of fine-tuning the perovskite composition and structure depending on the application.

4 Conclusion

The effect of copper doping at the B-site of $\text{Sr}_{0.85}\text{Ce}_{0.15}\text{Fe}_{0.67}\text{Co}_{0.33-x}\text{Cu}_x\text{O}_3$ perovskite oxides (SCFCC with $x=0.1, 0.2$) has been investigated in oxygen-related processes, evidencing how the physicochemical, catalytic and antibacterial properties of these perovskite oxides change upon different activation methods. Copper has a positive role in all the investigated processes, although it is not fully ascertained if its role is direct or indirect, through induction of the segregated CeO_2 phase and consequent perovskite oxide defectivity. The generation of ROS that can be maintained active also after removing the SCFCC powder and the source of excitation paves the way to the applicability of these materials also when the direct UV or thermal treatment on the target is not feasible. Although the versatility of perovskite oxides has been already known in the literature, important structure-properties relationships have been proposed and discussed. This work further evidenced the importance of the activation process in the functional use of perovskite oxide materials, and can serve as an inspiration for future research works on perovskite oxides for environmental and energy applications.

Data availability statement

All relevant data is contained within the article: The original contributions presented in the study are included in the article/supplementary material, further inquiries can be directed to the corresponding author.

Author contributions

MT contributed to the conception of the study and wrote the first draft of the manuscript; MT, CV, AV, LL, MR, EL, and FD performed the experimental trials; FD, LL, and EL wrote sections of the manuscript. All authors contributed to the article and approved the submitted version.

Funding

This study was carried out within the MICS (Made in Italy—Circular and Sustainable) Extended Partnership and received funding from the European Union Next-GenerationEU [Piano Nazionale di Ripresa e Resilienza (PNRR)—Missione 4 Componente 2, Investimento 1.3—D.D. 1551.11-10-2022, PE00000004].

Acknowledgments

We are grateful to Orion Engineered Carbons GmbH and the distributor Eigenmann & Veronelli SPA for providing Carbon

References

- Abd El-Naser, A., Abdel-Khalek, E. K., Nabhan, E., Rayan, D. A., Gaafar, M. S., and Abd El-Aal, N. S. (2021). Study the influence of oxygen-deficient ($\delta = 0.135$) in SrFeO_{3- δ} nanoparticles perovskite on structural, electrical and magnetic properties. *Philos. Mag.* 101, 710–728. doi:10.1080/14786435.2020.1862427
- Abdel-Khalek, E. K., Rayan, D. A., Askar, A. A., Maksoud, M. I. A. A., and El-Bahnasawy, H. H. (2021). Synthesis and characterization of SrFeO_{3- δ} nanoparticles as antimicrobial agent. *J. Sol-Gel Sci. Technol.* 97, 27–38. doi:10.1007/s10971-020-05431-8
- Ahmad, T., Farooq, U., and Phul, R. (2018). Fabrication and photocatalytic applications of perovskite materials with special emphasis on alkali-metal-based niobates and tantalates. *Ind. Eng. Chem. Res.* 57, 18–41. doi:10.1021/acs.iecr.7b04641
- Ali, S., Wu, X., Zuhra, Z., Ma, Y., Abbas, Y., Jin, B., et al. (2020). Cu-Mn-Ce mixed oxides catalysts for soot oxidation and their mechanistic chemistry. *Appl. Surf. Sci.* 512, 145602. doi:10.1016/j.apsusc.2020.145602
- Amar, I. A., Lan, R., and Tao, S. (2015). Synthesis of ammonia directly from wet nitrogen using a redox stable La_{0.75}Sr_{0.25}Cr_{0.5}Fe_{0.5}O_{3- δ} -Ce_{0.8}Gd_{0.18}Ca_{0.02}O_{2- δ} composite cathode. *RSC Adv.* 5, 38977–38983. doi:10.1039/c5ra00600g
- Amaveda, H., Madre, M. A., Mora, M., Torres, M. A., and Sotelo, A. (2023). Anomalous grain growth in sintered Bi₂Ca₂Co_{2-x}Cu_xO_y + Ag ceramic composites by Cu doping. *J. Mat. Sci. Mat. Electron.* 34, 9–8. doi:10.1007/s10854-022-09416-x
- Aneggi, E., Divins, N. J., De Leitenburg, C., Llorca, J., and Trovarelli, A. (2014). The formation of nanodomains of Ce₆O₁₁ in ceria catalyzed soot combustion. *J. Catal.* 312, 191–194. doi:10.1016/j.jcat.2014.01.020
- Bendieb Aberkane, A., Yeste, M. P., Fayçal, D., Goma, D., and Cauqui, M. Á. (2019). Catalytic soot oxidation activity of NiO-CeO₂ catalysts prepared by a coprecipitation method: influence of the preparation pH on the catalytic performance. *Mater. (Basel)* 12, 3436. doi:10.3390/ma12203436
- Bianco Prevot, A., Fabbri, D., Bernardini, E., Deganello, F., Tummino, M. L., and Magnacca, G. (2021). “Insights on the photocatalytic performances of LaFeO₃ synthesized by solution combustion synthesis,” in *Materials science in photocatalysis* (China: Elsevier), 357–370. doi:10.1016/B978-0-12-821859-4.00023-4
- Black. The authors are grateful to the CNR-ISMN Palermo technician Francesco Giordano for XRD measurements. We thank Dr. Roberta Peila and Dr. Cinzia Tonetti for helping during ICP measurements.
- Blosi, M., Costa, A. L., Ortelli, S., Belosi, F., Ravegnani, F., Varesano, A., et al. (2021). Polyvinyl alcohol/silver electrospun nanofibers: biocidal filter media capturing virus-size particles. *J. Appl. Polym. Sci.* 138, 51380. doi:10.1002/app.51380
- Bonura, L., Bianchi, G., Sanchez Ramirez, D. O., Carletto, R. A., Varesano, A., Vineis, C., et al. (2019). “Monitoring systems of an electrospinning plant for the production of composite nanofibers,” in *Factories of the future*. Editors T. Tolio, G. Copani, and W. Terkaj (Cham: Springer International Publishing), 315–337. doi:10.1007/978-3-319-94358-9_15
- Bueno-López, A. (2014). Diesel soot combustion ceria catalysts. *Appl. Catal. B Environ.* 146, 1–11. doi:10.1016/j.apcatb.2013.02.033
- Bueno-López, A. (2015). “Progresses on soot combustion perovskite catalysts,” in *Perovskites and related mixed oxides* (Weinheim, Germany: Wiley-VCH Verlag GmbH & Co. KGaA), 437–450. doi:10.1002/9783527686605.ch19
- Bulemo, P. M., and Kim, I. D. (2020). Recent advances in ABO₃ perovskites: their gas-sensing performance as resistive-type gas sensors. *J. Korean Ceram. Soc.* 57, 24–39. doi:10.1007/s43207-019-00003-1
- Cao, J., Ji, Y., and Shao, Z. (2022). Perovskites for protonic ceramic fuel cells: a review. *Energy Environ. Sci.* 15, 2200–2232. doi:10.1039/d2ee00132b
- Cho, E. C., Chang-Jian, C. W., Huang, J. H., Lee, G. Y., Hung, W. H., Sung, M. Y., et al. (2021). Co₂₊-Doped BiOBrxCl_{1-x} hierarchical microspheres display enhanced visible-light photocatalytic performance in the degradation of rhodamine B and antibiotics and the inactivation of *E. coli*. *J. Hazard. Mater.* 402, 123457. doi:10.1016/j.jhazmat.2020.123457
- Cowin, P. I., Lan, R., Petit, C. T. G., Du, D., Xie, K., Wang, H., et al. (2017). Conductivity and redox stability of new perovskite oxides SrFe_{0.7}Ti_{0.2}Mn_{0.1}O_{3- δ} (TM = Mn, Fe, Co, Ni, Cu). *Solid State Ionics* 301, 99–105. doi:10.1016/j.ssi.2017.01.017
- Das, N., and Kandimalla, S. (2017). Application of perovskites towards remediation of environmental pollutants: an overview: a review on remediation of environmental pollutants using perovskites. *Int. J. Environ. Sci. Technol.* 14, 1559–1572. doi:10.1007/s13762-016-1233-7

Conflict of interest

The author MT declared that they were an editorial board member of Frontiers, at the time of submission. This had no impact on the peer review process and the final decision.

The remaining authors declare that the research was conducted in the absence of any commercial or financial relationships that could be construed as a potential conflict of interest.

Publisher's note

All claims expressed in this article are solely those of the authors and do not necessarily represent those of their affiliated organizations, or those of the publisher, the editors and the reviewers. Any product that may be evaluated in this article, or claim that may be made by its manufacturer, is not guaranteed or endorsed by the publisher.

Author disclaimer

This manuscript reflects only the authors' views and opinions, neither the European Union nor the European Commission can be considered responsible for them.

- Deganello, F., Liotta, L. F., Longo, A., Casaletto, M. P., and Scopelliti, M. (2006). Cerium effect on the phase structure, phase stability and redox properties of Ce-doped strontium ferrates. *J. Solid State Chem.* 179, 3406–3419. doi:10.1016/j.jssc.2006.06.027
- Deganello, F., Marci, G., and Deganello, G. (2009). Citrate-nitrate auto-combustion synthesis of perovskite-type nanopowders: a systematic approach. *J. Eur. Ceram. Soc.* 29, 439–450. doi:10.1016/j.jeurceramsoc.2008.06.012
- Deganello, F., Oko, D. N., Testa, M. L., La Parola, V., Tummino, M. L., Soares, C. O., et al. (2018). Perovskite-type catalysts prepared by nanocasting: effect of metal silicates on the electrocatalytic activity toward oxygen evolution and reduction reactions. *ACS Appl. Energy Mat.* 1, 2565–2575. doi:10.1021/acsaem.8b00282
- Deganello, F., Tummino, M. L., Calabrese, C., Testa, M. L., Avetta, P., Fabbri, D., et al. (2015). A new, sustainable LaFeO₃ material prepared from biowaste-sourced soluble substances. *New J. Chem.* 39, 877–885. doi:10.1039/c4nj01279h
- Deganello, F., and Tyagi, A. K. (2018). Solution combustion synthesis, energy and environment: best parameters for better materials. *Prog. Cryst. Growth Charact. Mater.* 64, 23–61. doi:10.1016/j.pcrysgrow.2018.03.001
- Deng, H., Lin, L., and Liu, S. (2010). Catalysis of Cu-doped Co-based perovskite-type oxide in wet oxidation of lignin to produce aromatic aldehydes. *Energy & Fuels* 24, 4797–4802. doi:10.1021/ef100768e
- Dhakad, M., Rayalu, S. S., Kumar, R., Doggali, P., Bakardjieva, S., Subrt, J., et al. (2008). Low cost, ceria promoted perovskite type catalysts for diesel soot oxidation. *Catal. Lett.* 121, 137–143. doi:10.1007/s10562-007-9310-7
- Eichel, R. A., Kungl, H., and Jakes, P. (2013). Defect structure of non-stoichiometric and aliovalently doped perovskite oxides. *Mater. Technol.* 28, 241–246. doi:10.1179/175355513X13715615193120
- Ejmont, A., Jankowska, A., and Goscianska, J. (2022). Insight into the photocatalytic activity of cobalt-based metal-organic frameworks and their composites. *Catalysts* 12, 110. doi:10.3390/catal12020110
- El Mragui, A., Zegaoui, O., and Esteves da Silva, J. C. G. (2021). Elucidation of the photocatalytic degradation mechanism of an azo dye under visible light in the presence of cobalt doped TiO₂ nanomaterials. *Chemosphere* 266, 128931. doi:10.1016/j.chemosphere.2020.128931
- Farr, T. P., Nguyen, N. P., Bush, H. E., Ambrosini, A., and Loutzenhiser, P. G. (2020). Perovskites for solar thermochemical air separation. *Materials* 13 (22), 5123. doi:10.3390/ma13225123
- Fernández-Ropero, A. J., Porras-Vázquez, J. M., Cabeza, A., Slater, P. R., Marrero-López, D., and Losilla, E. R. (2014). High valence transition metal doped strontium ferrites for electrode materials in symmetrical SOFCs. *J. Power Sources* 249, 405–413. doi:10.1016/j.jpowsour.2013.10.118
- Fox, E. B., Lee, A. F., Wilson, K., and Song, C. (2008). *In-situ* XPS study on the reducibility of Pd-promoted Cu/CeO₂ catalysts for the oxygen-assisted water-gas-shift reaction. *Top. Catal.* 49, 89–96. doi:10.1007/s11244-008-9063-6
- Frew, J. E., Jones, P., and Scholes, G. (1983). Spectrophotometric determination of hydrogen peroxide and organic hydroperoxides at low concentrations in aqueous solution. *Anal. Chim. Acta* 155, 139–150. doi:10.1016/S0003-2670(00)85587-7
- Gainutdinov, I. I., Nemudry, A. P., and Zilberberg, I. L. (2019). The influence of A- and B-cation substitution on electronic structure of SrFeO₃ and SrCoO₃. *Mater. Today Proc.* 12, 21–24. doi:10.1016/j.matpr.2019.02.208
- Garbarz-Glos, B., Bąk, W., Kalvane, A., Antonova, M., and Klimkowski, G. (2019). Effects of CuO doping on structure, microstructure and dielectric properties of BaTiO₃-PbTiO₃ solid solution. *Integr. Ferroelectr.* 196, 70–77. doi:10.1080/10584587.2019.1591961
- García-López, E., Marci, G., Puleo, F., La Parola, V., and Liotta, L. F. (2015). La_{1-x}Sr_xCo_{1-y}Fe_yO_{3-δ} perovskites: preparation, characterization and solar photocatalytic activity. *Appl. Catal. B Environ.* 178, 218–225. doi:10.1016/j.apcatb.2014.09.014
- Górecka, S., Pacultová, K., Smýkalová, A., Fridrichová, D., Górecki, K., Rokicińska, A., et al. (2022). Role of the Cu content and Ce activating effect on catalytic performance of Cu-Mg-Al and Ce/Cu-Mg-Al oxides in ammonia selective catalytic oxidation. *Appl. Surf. Sci.* 573, 151540. doi:10.1016/j.apsusc.2021.151540
- Grabowska, E. (2016). Selected perovskite oxides: characterization, preparation and photocatalytic properties-A review. *Appl. Catal. B Environ.* 186, 97–126. doi:10.1016/j.apcatb.2015.12.035
- Guo, Q., Li, X., Wei, H., Liu, Y., Li, L., Yang, X., et al. (2019). Sr, Fe co-doped perovskite oxides with high performance for oxygen evolution reaction. *Front. Chem.* 7, 224–228. doi:10.3389/fchem.2019.00224
- Gupta, S., Fernandes, R., Patel, R., Spreitzer, M., and Patel, N. (2023). A review of cobalt-based catalysts for sustainable energy and environmental applications. *Appl. Catal. A General* 661, 119254. doi:10.1016/j.apcata.2023.119254
- He, F., Jeon, W., and Choi, W. (2021a). Photocatalytic air purification mimicking the self-cleaning process of the atmosphere. *Nat. Commun.* 12, 2528. doi:10.1038/s41467-021-22839-0
- He, J., Yao, P., Qiu, J., Zhang, H., Jiao, Y., Wang, J., et al. (2021b). Enhancement effect of oxygen mobility over Ce_{0.5}Zr_{0.5}O₂ catalysts doped by multivalent metal oxides for soot combustion. *Fuel* 286, 119359. doi:10.1016/j.fuel.2020.119359
- Hoang, V. Q. T., Phan, T. Q. P., Senthilkumar, V., Doan, V. T., Kim, Y. S., and Le, M. V. (2019). Enhanced photocatalytic activities of vanadium and molybdenum co-doped strontium titanate under visible light. *Int. J. Appl. Ceram. Technol.* 16, 1651–1658. doi:10.1111/ijac.13248
- Huang, X., Zhao, G., Chang, Y., Wang, G., and Irvine, J. T. S. (2018). Nanocrystalline CeO₂-δ coated β-MnO₂ nanorods with enhanced oxygen transfer property. *Appl. Surf. Sci.* 440, 20–28. doi:10.1016/j.apsusc.2017.12.197
- Ikeda, H., Nikata, S., Hirakawa, E., Tsuchida, A., and Miura, N. (2016). Oxygen sorption/desorption behavior and crystal structural change for SrFeO_{3-δ}. *Chem. Eng. Sci.* 147, 166–172. doi:10.1016/j.ces.2016.03.034
- Ishihara, T. (2017). “Inorganic perovskite oxides,” in *Electronic and photonic materials springer handbooks*. Editors S. Kasap and P. Capper (Cham: Springer International Publishing), 1405–1420. doi:10.1007/978-3-319-48933-9_59
- Jaison, A., Mohan, A., and Lee, Y. C. (2023). Recent developments in photocatalytic nanotechnology for purifying air polluted with volatile organic compounds: effect of operating parameters and catalyst deactivation. *Catalysts* 13, 407. doi:10.3390/catal13020407
- Janowska, K., Boffa, V., Jørgensen, M. K., Quist-Jensen, C. A., Hubac, F., Deganello, F., et al. (2020). Thermocatalytic membrane distillation for clean water production. *npj Clean. Water* 3, 34–37. doi:10.1038/s41545-020-00082-2
- Jeong, M. G., Park, E. J., Seo, H. O., Kim, K. D., Kim, Y. D., and Lim, D. C. (2013). Humidity effect on photocatalytic activity of TiO₂ and regeneration of deactivated photocatalysts. *Appl. Surf. Sci.* 271, 164–170. doi:10.1016/j.apsusc.2013.01.155
- Ji, Q., Bi, L., Zhang, J., Cao, H., and Zhao, X. S. (2020). The role of oxygen vacancies of ABO₃ perovskite oxides in the oxygen reduction reaction. *Energy Environ. Sci.* 13, 1408–1428. doi:10.1039/D0EE00092B
- Kang, H. W., Lim, S. N., Park, S. Bin, and Park, A. H. A. (2013). H₂ evolution under visible light irradiation on La and Cr co-doped NaTaO₃ prepared by spray pyrolysis from polymeric precursor. *Int. J. Hydrogen Energy* 38, 6323–6334. doi:10.1016/j.ijhydene.2013.03.048
- Kastrinaki, G., Lorentzou, S., and Konstandopoulos, A. G. (2015). Soot oxidation kinetics of different ceria nanoparticle catalysts. *Emiss. Control Sci. Technol.* 1, 247–253. doi:10.1007/s40825-015-0021-z
- Kaur, P., and Singh, K. (2020). Review of perovskite-structure related cathode materials for solid oxide fuel cells. *Ceram. Int.* 46, 5521–5535. doi:10.1016/j.ceramint.2019.11.066
- Khalil, K. M. S., Elkabee, L. A., and Murphy, B. (2005). Preparation and characterization of thermally stable porous ceria aggregates formed via a sol-gel process of ultrasonically dispersed cerium(IV) isopropoxide. *Microporous Mesoporous Mater.* 78, 83–89. doi:10.1016/j.micromeso.2004.09.019
- Khiraide, P., and Raut, V. (2022). “Perovskite structured materials: synthesis, structure, physical properties and applications,” in *Recent advances in multifunctional perovskite materials* (China: IntechOpen). doi:10.5772/intechopen.106252
- Khobragade, R., Saravanan, G., Einaga, H., Nagashima, H., Shukla, P., Gupta, T., et al. (2021). Diesel fuel particulate emission control using low-cost catalytic materials. *Fuel* 302, 121157. doi:10.1016/j.fuel.2021.121157
- Kotomin, E. A., Kuzmin, A., Purans, J., Timoshenko, J., Piskunov, S., Merkle, R., et al. (2022). Theoretical and experimental studies of charge ordering in CaFeO₃ and SrFeO₃ crystals. *Phys. status solidi (b)* 259, 2100238–2100246. doi:10.1002/psb.202100238
- Kwon, O., Joo, S., Choi, S., Sengodan, S., and Kim, G. (2020). Review on exsolution and its driving forces in perovskites. *JPhys Energy* 2, 032001. doi:10.1088/2515-7655/ab8c1f
- Li, B., He, S., Li, J., Yue, X., Irvine, J. T. S., Xie, D., et al. (2020). A Ce/Ru codoped SrFeO_{3-δ} perovskite for a coke-resistant anode of a symmetrical solid oxide fuel cell. *ACS Catal.* 10, 14398–14409. doi:10.1021/acscatal.0c03554
- Li, B., Raj, A., Croiset, E., and Wen, J. Z. (2019a). Reactive Fe-O-Ce sites in ceria catalysts for soot oxidation. *Catalysts* 9, 815–822. doi:10.3390/catal9100815
- Li, J., Ma, W., Zhong, D., Li, K., Ma, J., Zhang, S., et al. (2022). Oxygen vacancy concentration modulation of perovskite-based heterogeneous catalysts for Fenton-like oxidation of tetracycline. *J. Clean. Prod.* 362, 132469. doi:10.1016/j.jclepro.2022.132469
- Li, J., Zhong, D., Huang, J., Ma, W., Li, K., Li, M., et al. (2023a). Cobalt mediated perovskite as efficient Fenton-like catalysts for the tetracycline removal over a neutral condition: the importance of superoxide radical. *Chemosphere* 313, 137564. doi:10.1016/j.chemosphere.2022.137564
- Li, S., Hao, X., Abudula, A., and Guan, G. (2019b). Nanostructured Co-based bifunctional electrocatalysts for energy conversion and storage: current status and perspectives. *J. Mat. Chem. A* 7, 18674–18707. doi:10.1039/C9TA04949E
- Li, W., Li, M., Guo, Y., Hu, Z., Zhou, C., Brand, H. E. A., et al. (2023b). High cationic dispersity boosted oxygen reduction reactivity in multi-element doped perovskites. *Adv. Funct. Mater.* 33, 2210496. doi:10.1002/adfm.202210496
- Li, X., and Gao, H. (2018). Role of ceria in the improvement of NO removal of lanthanum-based perovskite-Type catalysts. *RSC Adv.* 8, 11778–11784. doi:10.1039/c8ra00456k

- Liang, P., Meng, D., Liang, Y., Wang, Z., Zhang, C., Wang, S., et al. (2021). Cation deficiency tuned LaCoO₃-δ perovskite for peroxymonosulfate activation towards bisphenol A degradation. *Chem. Eng. J.* 409, 128196. doi:10.1016/j.cej.2020.128196
- Lim, P. F., Leong, K. H., Sim, L. C., Saravanan, P., and Aziz, A. A. (2019). Perovskite oxide-based photocatalysts for excellent visible light-driven photocatalysis and energy conversion. *Plant Nanobionics*, 35–54. doi:10.1007/978-3-030-16379-2_2
- Liu, J., Jiang, Z., Servati, P., and Asselin, E. (2016). Etching induced stepped nanostructure on Pb(Mg_(1-x/2)Mn_(x/2)W_{1/2})O₃Ceramics. *J. Am. Ceram. Soc.* 99, 1125–1128. doi:10.1111/jace.14167
- Liu, Y., Baumann, S., Schulze-Küppers, F., Mueller, D. N., and Guillon, O. (2018). Co and Fe co-doping influence on functional properties of SrTiO₃ for use as oxygen transport membranes. *J. Eur. Ceram. Soc.* 38, 5058–5066. doi:10.1016/j.jeurceramsoc.2018.07.037
- Lopez-Romero, J. C., González-Ríos, H., Borges, A., and Simões, M. (2015). Antibacterial effects and mode of action of selected essential oils components against *Escherichia coli* and *Staphylococcus aureus*. *Evidence-Based Complementary Altern. Med.* 2015, 1–9. doi:10.1155/2015/795435
- Lu, L., Ni, C., Cassidy, M., and Irvine, J. T. S. (2016). Demonstration of high performance in a perovskite oxide supported solid oxide fuel cell based on La and Ca co-doped SrTiO₃. *J. Mat. Chem. A* 4, 11708–11718. doi:10.1039/c6ta04074h
- Lu, Z., Shen, J., Zou, J., Zhang, Q., Mo, J., Wu, Z., et al. (2023). Mössbauer spectroscopic analysis of La_{1-x}Sr_xFeO_{3-δ} perovskites. *Phys. status solidi (b)* 260, 1–5. doi:10.1002/psb.202200511
- Mabate, T. P., Maqunga, N. P., Ntshibongo, S., Maumela, M., and Bingwa, N. (2023). Metal oxides and their roles in heterogeneous catalysis: special emphasis on synthesis protocols, intrinsic properties, and their influence in transfer hydrogenation reactions. *SN Appl. Sci.* 5, 196. doi:10.1007/s42452-023-05416-6
- Mahofa, E. P., Narsaiah, T. B., and Chakra, C. S. (2018). Catalytic soot oxidation using ceria, cobalt and copper nanocomposites. *MRS Adv.* 3, 2581–2588. doi:10.1557/adv.2018.286
- Maleki Rizzi, M. H., Aghabari, B., Alizadeh, M., Khanlarkhani, A., and Martinez Huerta, M. V. (2019). The role of cobalt and copper nanoparticles on performance of magnetite-rich waste material in Fenton reaction. *Int. J. Environ. Sci. Technol.* 16, 373–382. doi:10.1007/s13762-017-1579-5
- Mamba, G., Mafa, P. J., Muthuraj, V., Mashayekh-Salehi, A., Royer, S., Nkambule, T. I. T., et al. (2022). Heterogeneous advanced oxidation processes over stoichiometric ABO₃ perovskite nanostructures. *Mater. Today Nano* 18, 100184. doi:10.1016/j.mtnano.2022.100184
- Meng, D., Gu, H., Lu, Q., Zhao, Y., Zhu, G., Zhang, Y., et al. (2021). Advances and perspectives for the application of perovskite oxides in supercapacitors. *Energy & Fuels* 35, 17353–17371. doi:10.1021/acs.energyfuels.1c03157
- Mi, J., Chen, J., Chen, X., Liu, X., and Li, J. (2023). Recent status and developments of vacancies modulation in the ABO₃ perovskites for catalytic applications. *Chem. (Weinheim der Bergstrasse, Ger.)* 29, e202202713. doi:10.1002/chem.202202713
- Miceli, P., Bensaïd, S., Russo, N., and Fino, D. (2015). Effect of the morphological and surface properties of CeO₂-based catalysts on the soot oxidation activity. *Chem. Eng. J.* 278, 190–198. doi:10.1016/j.cej.2014.10.055
- Mohammed, J., Tchouank Tekou Carol, T., Mukhtar, G., Kumar, V., Bhadu, G. R., Godara, S. K., et al. (2020). Phase structure evolution, crystal structure refinement, morphology, and electro-optical properties of heat-treated Ca_{0.9}Ni_{0.1}Cu₂La_{0.1}Ti₄O₁₂. *Ceram. Int.* 46, 7187–7197. doi:10.1016/j.ceramint.2019.11.213
- Monama, G. R., Ramohlola, K. E., Iwuoha, E. I., and Modibane, K. D. (2022). Progress on perovskite materials for energy application. *Results Chem.* 4, 100321. doi:10.1016/j.rechem.2022.100321
- Nagrare, B. S., and Bhoga, S. S. (2010). Investigation on structure and electrical property of perovskite type Ba_xSr_{1-x}Co_{0.6}Fe_{0.4}O_{3-δ} (x = 0.2–0.8) oxides. *Integr. Ferroelectr.* 116, 101–112. doi:10.1080/10584587.2010.488579
- Neagu, D., Kyriakou, V., Roiban, I. L., Aouine, M., Tang, C., Caravaca, A., et al. (2019). *In situ* observation of nanoparticle exsolution from perovskite oxides: from atomic scale mechanistic insight to nanostructure tailoring. *ACS Nano* 13, 12996–13005. doi:10.1021/acsnano.9b05652
- Neagu, D., Tsekouras, G., Miller, D. N., Ménard, H., and Irvine, J. T. S. (2013). *In situ* growth of nanoparticles through control of non-stoichiometry. *Nat. Chem.* 5, 916–923. doi:10.1038/nchem.1773
- Njoku, C. B., Oseghe, E., and Msagati, T. A. M. (2022). Synthesis and application of perovskite nanoparticles for the adsorption of ketoprofen and fenoprofen in wastewater for sustainable water management. *J. Mol. Liq.* 346, 118232. doi:10.1016/j.molliq.2021.118232
- Østergaard, M. B., Deganello, F., La Parola, V., Liotta, L. F., Boffa, V., and Jørgensen, M. K. (2023). Beneficial effect of cerium excess on *in situ* grown Sr_{0.86}Ce_{0.14}FeO_{3-δ}-CeO₂ thermocatalysts for the degradation of bisphenol A. *RSC Adv.* 13, 21459–21470. doi:10.1039/D3RA03404F
- Østergaard, M. B., Strunck, A. B., Boffa, V., and Jørgensen, M. K. (2022). Kinetics of strontium carbonate formation on a Ce-doped SrFeO₃ perovskite. *Catalysts* 12, 265. doi:10.3390/catal12030265
- Østergaard, M. B., Strunck, A. B., Jørgensen, M. K., and Boffa, V. (2021). Abatement of oil residues from produced water using a thermocatalytic packed bed reactor. *J. Environ. Chem. Eng.* 9, 106749–106755. doi:10.1016/j.jece.2021.106749
- Palma, D., Deganello, F., Liotta, L. F., La Parola, V., Bianco Prevot, A., Malandrino, M., et al. (2023). Main issues in the synthesis and testing of thermocatalytic Ce-doped SrFeO₃ perovskites for wastewater pollutant removal. *Inorganics* 11, 85–18. doi:10.3390/inorganics11020085
- Park, J., Xu, B., Pan, J., Zhang, D., Lany, S., Liu, X., et al. (2023). Accurate prediction of oxygen vacancy concentration with disordered A-site cations in high-entropy perovskite oxides. *npj Comput. Mat.* 9, 29. doi:10.1038/s41524-023-00981-1
- Parmar, D. D., Dhruv, P. N., Meena, S. S., Kavita, S., Sandhu, C. S., Ellouze, M., et al. (2020). Effect of copper substitution on the structural, magnetic, and dielectric properties of M-type lead hexaferrite. *J. Electron. Mater.* 49, 6024–6039. doi:10.1007/s11664-020-08326-0
- Parrino, F., García-López, E., Marci, G., Palmisano, L., Felice, V., Sora, I. N., et al. (2016). Cu-substituted lanthanum ferrite perovskites: preparation, characterization and photocatalytic activity in gas-solid regime under simulated solar light irradiation. *J. Alloys Compd.* 682, 686–694. doi:10.1016/j.jallcom.2016.05.017
- Ponraj, C., Kumar, P. S., Sarkar, S., Krishnamoorthi, C., Manikandan, N., Vinitha, G., et al. (2022). Enhanced visible light photocatalytic activity of magnetic cobalt doped BiFeO₃. *Surfaces Interfaces* 31, 102050. doi:10.1016/j.surfin.2022.102050
- Prakash, A., and Jalan, B. (2019). Wide bandgap perovskite oxides with high room-temperature electron mobility. *Adv. Mat. Interfaces* 6, 1900479–1900514. doi:10.1002/admi.201900479
- Qi, M., Li, W., Zheng, X., Li, X., Sun, Y., Wang, Y., et al. (2020). Cerium and its oxidant-based nanomaterials for antibacterial applications: a state-of-the-art review. *Front. Mat.* 7, 1–26. doi:10.3389/fmats.2020.00213
- Rao, K. N., Venkataswamy, P., and Reddy, B. M. (2011). Structural characterization and catalytic evaluation of supported copper-ceria catalysts for soot oxidation. *Ind. Eng. Chem. Res.* 50, 11960–11969. doi:10.1021/ie201474p
- Reddy, B. M., Bharali, P., Thirumurthulu, G., Saikia, P., Katta, L., and Park, S. E. (2008). Catalytic efficiency of ceria-zirconia and ceria-hafnia nanocomposite oxides for soot oxidation. *Catal. Lett.* 123, 327–333. doi:10.1007/s10562-008-9427-3
- Renaudin, G., Gomes, S., and Nedelec, J. M. (2017). First-row transition metal doping in calcium phosphate bioceramics: a detailed crystallographic study. *Mater. (Basel)* 10, 92. doi:10.3390/ma10010092
- Rojas-Cervantes, M. L., and Castillejos, E. (2019). Perovskites as catalysts in advanced oxidation processes for wastewater treatment. *Catalysts* 9, 230. doi:10.3390/catal9030230
- Royer, S., Duprez, D., Can, F., Courtois, X., Batiot-Dupeyrat, C., Laassiri, S., et al. (2014). Perovskites as substitutes of noble metals for heterogeneous catalysis: dream or reality. *Chem. Rev.* 114, 10292–10368. doi:10.1021/cr500032a
- Saadatkhan, N., Carillo Garcia, A., Ackermann, S., Leclerc, P., Latifi, M., Samih, S., et al. (2020). Experimental methods in chemical engineering: thermogravimetric analysis—Tga. *Can. J. Chem. Eng.* 98, 34–43. doi:10.1002/cjce.23673
- Salah, I., Parkin, I. P., and Allan, E. (2021). Copper as an antimicrobial agent: recent advances. *RSC Adv.* 11, 18179–18186. doi:10.1039/D1RA02149D
- Salazar, R., Brillas, E., and Sirés, I. (2012). Finding the best Fe²⁺/Cu²⁺ combination for the solar photoelectro-Fenton treatment of simulated wastewater containing the industrial textile dye Disperse Blue 3. *Appl. Catal. B Environ.* 115–116, 107–116. doi:10.1016/j.apcatb.2011.12.026
- Sharma, S., Kumar, R., Raizada, P., Ahamad, T., Alshehri, S. M., Nguyen, V. H., et al. (2022). An overview on recent progress in photocatalytic air purification: metal-based and metal-free photocatalysis. *Environ. Res.* 214, 113995. doi:10.1016/j.envres.2022.113995
- Sharmila, M., Mani, R. J., Parvathiraja, C., Kader, S. M. A., Siddiqui, M. R., Wabaidur, S. M., et al. (2022). Visible light photocatalyst and antibacterial activity of BFO (bismuth ferrite) nanoparticles from honey. *Water* 14, 1545. doi:10.3390/w14101545
- She, S., Zhu, Y., Wu, X., Hu, Z., Shelke, A., Pong, W. F., et al. (2022). Realizing high and stable electrocatalytic oxygen evolution for iron-based perovskites by Co-Doping-Induced structural and electronic modulation. *Adv. Funct. Mater.* 32, 2111091–2111110. doi:10.1002/adfm.202111091
- Shen, Q., Dong, S., Li, S., Yang, G., and Pan, X. (2021). A review on the catalytic decomposition of NO by perovskite-type oxides. *Catalysts* 11, 622. doi:10.3390/catal11050622
- Shi, H., Ding, Z., and Ma, G. (2016). Electrochemical performance of cobalt-free Nd_{0.5}Ba_{0.5}Fe_{1-x}Ni_xO_{3-δ} Cathode materials for intermediate temperature solid oxide fuel cells. *Fuel Cells* 16, 258–262. doi:10.1002/fuce.201500156
- Shokri, A., and Fard, M. S. (2022). A critical review in Fenton-like approach for the removal of pollutants in the aqueous environment. *Environ. Challenges* 7, 100534. doi:10.1016/j.envc.2022.100534
- Shomrat, N., Haviv, D., and Tsur, Y. (2014). The correlation between non-stoichiometry and charge compensation in perovskites. *J. Electroceramics* 33, 135–141. doi:10.1007/s10832-014-9975-4

- singh, C., and Rakesh, M. (2019). A new cost effective potassium based LaFeO₃ perovskite for antimicrobial application. *Int. J. ChemTech Res.* 12, 87–96. doi:10.20902/IJCTR.2019.120510
- Singh, C., Wagle, A., and Rakesh, M. (2017). Doped LaCoO₃ perovskite with Fe: a catalyst with potential antibacterial activity. *Vacuum* 146, 468–473. doi:10.1016/j.vacuum.2017.06.039
- Singh, M., and Singh, A. K. (2020). Studies on structural, morphological, and electrical properties of Ga³⁺ and Cu²⁺ co-doped ceria ceramics as solid electrolyte for IT-SOFCs. *Int. J. Hydrogen Energy* 45, 24014–24025. doi:10.1016/j.ijhydene.2019.09.084
- Song, J., Zhu, T., Chen, X., Ni, W., and Zhong, Q. (2020). Cobalt and Titanium substituted SrFeO₃ based perovskite as efficient symmetrical electrode for solid oxide fuel cell. *J. Materomics* 6, 377–384. doi:10.1016/j.jmat.2020.02.009
- Souri, M., and Salar Amoli, H. (2023). Gas sensing mechanisms in ABO₃ perovskite materials at room temperature: A review. *Mater. Sci. Semicond. Process.* 156, 107271. doi:10.1016/j.mssp.2022.107271
- Su, C., Wang, W., and Shao, Z. (2021). Cation-deficient perovskites for clean energy conversion. *Accounts Mater. Res.* 2, 477–488. doi:10.1021/accountsmr.1c00036
- Su, C., Wang, Y., Kumar, A., and McGinn, P. J. (2018). Simulating real world soot-catalyst contact conditions for lab-scale catalytic soot oxidation studies. *Catalysts* 8, 247. doi:10.3390/catal8060247
- Sun, J., Zhao, Z., Li, Y., Yu, X., Zhao, L., Li, J., et al. (2020). Synthesis and catalytic performance of macroporous La_{1-x}Ce_xCoO₃ perovskite oxide catalysts with high oxygen mobility for catalytic combustion of soot. *J. Rare Earths* 38, 584–593. doi:10.1016/j.jre.2019.05.014
- Sun, Q., Sun, L., Dou, Y., Li, Q., Li, N., Huo, L., et al. (2021). Insights into the oxygen reduction reaction on Cu-doped SrFeO_{3-δ} cathode for solid oxide fuel cells. *J. Power Sources* 497, 229877–229879. doi:10.1016/j.jpowsour.2021.229877
- Sun, Y. F., Zhou, X. W., Zeng, Y., Amirkhiz, B. S., Wang, M. N., Zhang, L. Z., et al. (2015a). An ingenious Ni/Ce co-doped titanate based perovskite as a coking-tolerant anode material for direct hydrocarbon solid oxide fuel cells. *J. Mat. Chem. A* 3, 22830–22838. doi:10.1039/c5ta06200d
- Sun, Y., Li, J., Zeng, Y., Amirkhiz, B. S., Wang, M., Behnamian, Y., et al. (2015b). A-site deficient perovskite: the parent for *in situ* exsolution of highly active, regenerable nanoparticles as SOFC anodes. *J. Mat. Chem. A* 3, 11048–11056. doi:10.1039/c5ta01733e
- Suresh, S., Karthikeyan, S., and Jayamoorthy, K. (2016). FTIR and multivariate analysis to study the effect of bulk and nano copper oxide on peanut plant leaves. *J. Sci. Adv. Mater. Devices* 1, 343–350. doi:10.1016/j.jsamd.2016.08.004
- Taylor, F. H., Buckeridge, J., and Catlow, C. R. A. (2017). Screening divalent metals for A- and B-site dopants in LaFeO₃. *Chem. Mat.* 29, 8147–8157. doi:10.1021/acs.cemmater.7b01993
- Thomas, S., and Balakrishnan, P. (2020). in *Revolution of perovskite*. Editors N. S. Arul and V. D. Nithya Singapore (Springer Singapore). doi:10.1007/978-981-15-1267-4
- Toby, B. H. (2006). R factors in Rietveld analysis: how good is good enough? *Powder Diff.* 21, 67–70. doi:10.1154/1.2179804
- Toby, B. H., and Von Dreele, R. B. (2013). GSAS-II: the genesis of a modern open-source all purpose crystallography software package. *J. Appl. Crystallogr.* 46, 544–549. doi:10.1107/S0021889813003531
- Tonda, S., Kumar, S., Anjaneyulu, O., and Shanker, V. (2014). Synthesis of Cr and La-codoped SrTiO₃ nanoparticles for enhanced photocatalytic performance under sunlight irradiation. *Phys. Chem. Chem. Phys.* 16, 23819–23828. doi:10.1039/C4CP02963A
- Torregrosa-Rivero, V., Moreno-Marcos, C., Albaladejo-Fuentes, V., Sánchez-Adsuar, M. S., and Illán-Gómez, M. J. (2019). Bafel-xcuxo₃perovskites as active phase for diesel (Dpf) and gasoline particle filters (gpf). *Nanomaterials* 9, 1551. doi:10.3390/nano9111551
- Trofimenko, N. E., and Ullmann, H. (2000). Oxygen stoichiometry and mixed ionic-electronic conductivity of Sr_{1-x}Ce_xFe_{1-b}CoO_{3-x} perovskite-type oxides. *J. Eur. Ceram. Soc.* 20, 1241–1250. doi:10.1016/S0955-2219(99)00292-7
- Tummino, M. L., Laurenti, E., Deganello, F., Bianco Prevot, A., and Magnacca, G. (2017). Revisiting the catalytic activity of a doped SrFeO₃ for water pollutants removal: effect of light and temperature. *Appl. Catal. B Environ.* 207, 174–181. doi:10.1016/j.apcatb.2017.02.007
- Tummino, M. L., Liotta, L. F., Magnacca, G., Lo Faro, M., Trocino, S., Campagna Zignani, S., et al. (2020). Sucrose-Assisted solution combustion synthesis of doped strontium ferrate perovskite-type electrocatalysts: primary role of the secondary fuel. *Catalysts* 10, 134. doi:10.3390/catal10010134
- Tummino, M. L. (2022). SrFeO₃ peculiarities and exploitation in decontamination processes and environmentally-friendly energy applications. *Curr. Res. Green Sustain. Chem.* 5, 100339. doi:10.1016/j.crgsc.2022.100339
- Uppara, H. P., Dasari, H., Singh, S. K., Labhsetwar, N. K., and Murari, M. S. (2019). Effect of copper doping over GdFeO₃ perovskite on soot oxidation activity. *Catal. Lett.* 149, 3097–3110. doi:10.1007/s10562-019-02843-2
- Venkataswamy, P., Jampaiah, D., Mukherjee, D., and Reddy, B. M. (2019). CuO/Zn-CeO₂ nanocomposite as an efficient catalyst for enhanced diesel soot oxidation. *Emiss. Control Sci. Technol.* 5, 328–341. doi:10.1007/s40825-019-00137-y
- Vieten, J., Bulfin, B., Starr, D. E., Hariki, A., de Groot, F. M. F., Azarpira, A., et al. (2019). Redox behavior of solid solutions in the SrFe_{1-x}Cu_xO_{3-δ} system for application in thermochemical oxygen storage and air separation. *Energy Technol.* 7, 131–139. doi:10.1002/ente.201800554
- Villamena, F. A., Locigno, E. J., Rockenbauer, A., Hadad, C. M., and Zweier, J. L. (2006). Theoretical and experimental studies of the spin trapping of inorganic radicals by 5,5-dimethyl-1-pyrroline N-oxide (DMPO). 1. Carbon dioxide radical anion. *J. Phys. Chem. A* 110, 13253–13258. doi:10.1021/jp064892m
- Walton, R. I. (2020). Perovskite oxides prepared by hydrothermal and solvothermal synthesis: a review of crystallisation, chemistry, and compositions. *Chem. – A Eur. J.* 26, 9041–9069. doi:10.1002/chem.202000707
- Wang, B., Jin, M., An, H., Guo, Z., and Lv, Z. (2020). Hydrogenation performance of acetophenone to 1-phenylethanol on highly active nano Cu/SiO₂ catalyst. *Catal. Lett.* 150, 56–64. doi:10.1007/s10562-019-02908-2
- Wang, Q., Yuan, Y., Li, C., Zhang, Z., Xia, C., Pan, W., et al. (2023). Research progress on photocatalytic CO₂ reduction based on perovskite oxides. *Small* 2301892, 23018922–e2301925. doi:10.1002/smll.202301892
- Weon, S., He, F., and Choi, W. (2019). Status and challenges in photocatalytic nanotechnology for cleaning air polluted with volatile organic compounds: visible light utilization and catalyst deactivation. *Environ. Sci. Nano* 6, 3185–3214. doi:10.1039/c9en00891h
- Wolf, S. E., Winterhalder, F. E., Vibhu, V., de Haart, L. G. J., Guillon, O., Eichel, R.-A., et al. (2023). Solid oxide electrolysis cells – current material development and industrial application. *J. Mat. Chem. A* 6, 121. doi:10.1039/D3TA02161K
- Wu, H., and Zhu, X. (2016). Perovskite oxide nanocrystals — synthesis, characterization, functionalization, and novel applications, in *perovskite materials - synthesis, characterisation, properties, and applications*. InTech 6, 1. doi:10.5772/61640
- Wu, J. C. S., and Huang, C. W. (2010). *In situ* DRIFTS study of photocatalytic CO₂ reduction under UV irradiation. *Front. Chem. Eng. China* 4, 120–126. doi:10.1007/s11705-009-0232-3
- Xia, W., Lu, Y., and Zhu, X. (2020). Preparation methods of perovskite-type oxide materials. *Revolut. perovskite*, 61–93. doi:10.1007/978-981-15-1267-4_3
- Yang, J., and Guo, Y. (2018). Nanostructured perovskite oxides as promising substitutes of noble metals catalysts for catalytic combustion of methane. *Chin. Chem. Lett.* 29, 252–260. doi:10.1016/j.ccl.2017.09.013
- Yang, S., Wang, J., Chai, W., Zhu, J., and Men, Y. (2019). Enhanced soot oxidation activity over CuO/CeO₂ mesoporous nanosheets. *Catal. Sci. Technol.* 9, 1699–1709. doi:10.1039/c8cy02605j
- Yang, Y., Fang, J., Qin, Z., Pu, P., Yi, C., Yan, Y., et al. (2023). Performance of soot oxidation by O₂/NO/N₂ atmosphere in various catalyst species. *J. Therm. Anal. Calorim.* 148, 5709–5718. doi:10.1007/s10973-023-12110-7
- Yao, C., Zhang, H., Liu, X., Meng, J., Meng, J., and Meng, F. (2019). A niobium and tungsten co-doped SrFeO_{3-δ} perovskite as cathode for intermediate temperature solid oxide fuel cells. *Ceram. Int.* 45, 7351–7358. doi:10.1016/j.ceramint.2019.01.019
- Yu, J., Ran, R., Zhong, Y., Zhou, W., Ni, M., and Shao, Z. (2020). Advances in porous perovskites: synthesis and electrocatalytic performance in fuel cells and metal-air batteries. *Energy Environ. Mat.* 3, 121–145. doi:10.1002/eeem2.12064
- Zhang, H., Qin, H., Gao, C., Zhou, G., Chen, Y., and Hu, J. (2018). UV light illumination can improve the sensing properties of LaFeO₃ to acetone vapor. *Sensors Switz.* 18, 1990. doi:10.3390/s18071990
- Zhang, L., Tan, P. Y., Chow, C. L., Lim, C. K., Tan, O. K., Tse, M. S., et al. (2014). Antibacterial activities of mechanochemically synthesized perovskite strontium titanate ferrite metal oxide. *Colloids Surfaces A Physicochem. Eng. Aspects* 456, 169–175. doi:10.1016/j.colsurfa.2014.05.032
- Zhang, W., Niu, X., Chen, L., Yuan, F., and Zhu, Y. (2016). Soot combustion over nanostructured ceria with different morphologies. *Sci. Rep.* 6, 29062–29110. doi:10.1038/srep29062
- Zhang, X., Hu, J. Y., Dong, B. X., Li, X., Kou, S. Q., Zhang, S., et al. (2022). Effect of Cu and Zn elements on morphology of ceramic particles and interfacial bonding in TiB₂/Al composites. *Ceram. Int.* 48, 25894–25904. doi:10.1016/j.ceramint.2022.05.266
- Zhou, X.-W., Sun, Y.-F., Wang, G.-Y., Gao, T., Chuang, K. T., Luo, J.-L., et al. (2014). Synthesis and electrocatalytic performance of La_{0.3}Ce_{0.1}Sr_{0.5}Ba_{0.1}TiO₃ anode catalyst for solid oxide fuel cells. *Electrochem. Commun.* 43, 79–82. doi:10.1016/j.elecom.2014.03.019